

Chapter 6. Computer Simulation Algorithms

- 6.1 Introduction
- 6.2 Self Diffusion
- 6.3 Couette Flow and Shear Viscosity
- 6.4 Thermostatting shear flows.
- 6.5 Thermal conductivity
- 6.6 Norton ensemble methods - Self Diffusion
- 6.7 Constant Pressure Ensembles
- 6.8 The Constant Stress Ensemble

6.1 Introduction.

We will now show how linear response theory can be used to design computer simulation algorithms for the calculation of transport coefficients. There are two types of transport coefficients: mechanical and thermal. In this chapter we will show how thermal transport coefficients can be calculated using mechanical methods.

In nature nonequilibrium systems may respond essentially adiabatically, or depending upon circumstances, they may respond in an approximately isothermal manner - the quasi-isothermal response. No natural systems can be precisely adiabatic or isothermal. There will always be some transfer of the dissipative heat produced in nonequilibrium systems towards thermal boundaries. This heat may be radiated, convected or conducted to the boundary reservoir. Provided this heat transfer is slow on a microscopic timescale and provided that the temperature gradients implicit in the transfer process lead to negligible temperature differences on a microscopic length scale, we call the system *quasi-isothermal*. We assume that quasi-isothermal systems can be modelled on a microscopic scale in computer simulations, as isothermal systems.

In view of the robustness of the susceptibilities and equilibrium time correlation functions to various thermostating procedures (see §5.2,4), we expect that quasi-isothermal systems may be modelled using Gaussian or Nosé-Hoover thermostats or enostats. Furthermore, since heating effects are **quadratic** functions of the thermodynamic forces, the **linear** response of nonequilibrium systems can always be calculated by analysing, the adiabatic, the isothermal or the isoenergetic response.

Because of the fundamental relations between the linear nonequilibrium response and time dependent equilibrium fluctuations (Table 6.1) we have two ways of calculating the susceptibilities. We could perform an equilibrium simulation and calculate the appropriate equilibrium time correlation functions. The principle advantage of this method is that all possible transport coefficients can, in principle, be calculated from a single molecular dynamics run. This approach is however, very expensive in computer time with poor signal-to-noise ratios, and results that often depend strongly and nonmonotonically upon the size of the system being simulated. A frequently more useful approach is to perform a non-equilibrium simulation of the transport process. For mechanical transport processes we apply an external field, F_e , and calculate the transport coefficient L , from a linear constitutive relation:

$$L = \int_0^{\infty} dt \chi(t) = \lim_{F_e \rightarrow 0} \lim_{t \rightarrow \infty} \frac{\langle B(t) \rangle}{F_e} \quad (6.1.1)$$

The use of equation (6.1.1) necessitates a thermostat since otherwise, the work done on the system would be transformed continuously into heat and no steady state could be achieved (the limit, $t \rightarrow \infty$, would not exist). This method, known as non-equilibrium molecular dynamics (NEMD),

has the added advantage that it can, in principle, be used to calculate non-linear as well as linear transport coefficients. They can be calculated as a function of external field strength, frequency or wavevector. The most efficient, number independent way to calculate **mechanical** transport coefficients is to ignore the beautiful results of response theory and to duplicate the transport process, essentially as it occurs in nature.

Thermal transport processes are in principle much more difficult to simulate on the computer. A thermal transport process is one which is driven by boundary conditions rather than mechanical fields. For thermal processes we cannot perform time dependent perturbation theory because there is no external field appearing in the Hamiltonian which could be used as a perturbation variable. In spite of this difference, susceptibilities for thermal processes show many similarities to their mechanical counterparts (compare (5.3.8) with the results of Chapter 4). If J , is the flux of some conserved quantity (mass, momentum or energy) and if X is a gradient in the density of that conserved quantity, then a linear Navier-Stokes transport coefficient is defined by a constitutive relation of the form,

$$J = LX \tag{6.1.2}$$


In Chapter 4 we showed that each of the Navier-Stokes transport coefficients L , is related to equilibrium fluctuations by Green-Kubo relations. These relations are set out in Table 6.1. Remarkably Navier-Stokes thermal transport coefficients are related to equilibrium time correlation functions in essentially the same way as mechanical transport coefficients. We must stress however that this close formal similarity between thermal and mechanical transport coefficients only applies to Navier-Stokes thermal transport processes. If fluxes of non-conserved variables are involved, then Green-Kubo relations must be generalised (see equation (4.1.12) & §4.3). 

Table 6.1 Green-Kubo Relations for Navier-Stokes transport coefficients.

self diffusion

$$D = \frac{1}{3} \int_0^{\infty} dt \langle \mathbf{v}_i(t) \cdot \mathbf{v}_i(0) \rangle \quad (\text{T.6.1})$$

thermal conductivity

$$\lambda = \frac{V}{3k_B T^2} \int_0^{\infty} dt \langle \mathbf{J}_Q(t) \cdot \mathbf{J}_Q(0) \rangle \quad (\text{T.6.2})$$

shear viscosity

$$\eta = \frac{V}{k_B T} \int_0^{\infty} dt \langle P_{xy}(t) P_{xy}(0) \rangle \quad (\text{T.6.3})$$

bulk viscosity

$$\eta_v = \frac{1}{Vk_B T} \int_0^{\infty} dt \langle (p(t)V(t) - \langle pV \rangle) (p(0)V(0) - \langle pV \rangle) \rangle \quad (\text{T.6.4})$$

The ensemble averages employed in Table 6.1, are usually taken to be canonical while the time dependence of the correlation functions is generated by field free Newtonian equations of motion. In §5.4, we proved that, except for bulk viscosity, thermostatted equations of motion can also be used to generate the equilibrium time correlation functions. For bulk viscosity the correlation function involves functions of the kinetic energy of the system. We **cannot** therefore use Gaussian isokinetic equations of motion (see equation (5.4.7,8)). This is because, for these equations, the kinetic energy is a constant of the motion.

To calculate thermal transport coefficients using computer simulation we have the same two options that were available to us in the mechanical case. We could use equilibrium molecular dynamics to calculate the appropriate equilibrium time correlation functions, or we could mimic experiment as closely as possible and calculate the transport coefficients from their defining constitutive relations. Perhaps surprisingly the first technique to be used was equilibrium molecular dynamics (Alder and Wainwright, 1956). Much later the more efficient nonequilibrium approach was pioneered by Hoover and Ashurst (1975). Although the realistic nonequilibrium

approach proved more efficient than equilibrium simulations it was still far from ideal. This was because for thermal transport processes appropriate boundary conditions are needed to drive the system away from equilibrium - moving walls or walls maintained at different temperatures. These boundary conditions necessarily make the system inhomogeneous. In dense fluids particles pack against these walls, giving gives rise to significant number dependence and interpretative difficulties.

The most effective way to calculate thermal transport coefficients exploits the formal similarities between susceptibilities for thermal and mechanical transport coefficients. We **invent** a *fictitious* external field which interacts with the system in such a way as to precisely mimic the linear thermal transport process. The general procedure is outlined in Table 6.2. These methods are called 'synthetic' because the invented mechanical perturbation does not exist in nature. It is our invention and its purpose is to produce a precise mechanical analogue of a thermal transport process.

Table 6.2. Synthetic NEMD.

1. For the transport coefficient of interest L_{ij} , $J_i \equiv L_{ij}X_j$. Identify the Green Kubo relation for the transport coefficient,

$$L_{ij} = \int_0^{\infty} dt \langle J_i(t) J_j(0) \rangle$$

2. Invent a fictitious field F_e and its coupling to the system such that the dissipative flux

$$J \equiv \dot{H}_0^{\text{ad}} = J_j$$

3. Ensure $A\mathbf{\Gamma}$ is satisfied, that the equations of motion are homogeneous and that they are consistent with periodic boundary conditions.

4. Apply a thermostat.

5. Couple F_e to the system isothermally or isoenergetically and compute the steady state average, $\langle J_i(t) \rangle$, as a function of the external field, F_e . Linear response theory then proves,

$$L_{ij} = \lim_{F_e \rightarrow 0} \lim_{t \rightarrow \infty} \frac{\langle J_i(t) \rangle}{F_e}$$

With regard to step 3 in Table 6.2, it is not absolutely necessary to invent equations of motion which satisfy AIF (see §5.3). One can generalise response theory so that AIF is not required. However it is simpler and more convenient to require AIF and thus far it has always proved possible to generate algorithms which satisfy AIF. Although AIF is satisfied, most sets of equations of motion used in synthetic NEMD are not derivable from a Hamiltonian. The preferred algorithms for thermal conductivity and shear viscosity are not derivable from Hamiltonians. In the case of thermal conductivity the Hamiltonian approach must be abandoned because of conflicts with the periodic boundary condition convention used in simulations. For shear viscosity the breakdown of the Hamiltonian approach occurs for deeper reasons.

Equations of motion generated by this procedure are not unique, and it is usually not possible *a priori* to predict which particular algorithm will be most efficient. It is important to realise that the algorithms generated by this procedure are only guaranteed to lead to the correct **linear** ($\lim F_e \rightarrow 0$) transport coefficients. We have said nothing so far about generating the correct nonlinear response.

Many discussions of the relative advantages of NEMD and equilibrium molecular dynamics revolve around questions of efficiency. For large fields, NEMD is **orders of magnitude** more efficient than equilibrium molecular dynamics. On the other hand one can always make NEMD arbitrarily inefficient by choosing a sufficiently small field. At fields which are small enough for the response to be linear, there is no simple answer to the question of whether NEMD is more efficient than equilibrium MD. The number dependence of errors for the two methods are very different - compared to equilibrium MD, the relative accuracy of NEMD can be made arbitrarily great by increasing the system size.

These discussions of efficiency ignore two major advantages of NEMD over equilibrium molecular dynamics. Firstly, by simulating a **nonequilibrium** system one can visualise and study the microscopic physical mechanisms that are important to the transport processes (this is true both for synthetic and *realistic* NEMD). One can readily study the distortions of the local molecular structure of nonequilibrium systems. For molecular systems under shear, flow one can watch the shear induced processes of molecular alignment, rotation and conformational change (Edberg, Morriss and Evans, 1987). Obtaining this sort of information from equilibrium time correlation functions is possible but it is so difficult that no one has yet attempted the task. It is likely that no one ever will. Secondly, NEMD opens the door to studying the nonlinear response of systems far from equilibrium.

We will now give an extremely brief description of how one performs molecular dynamics simulations. We refer the reader to far more detailed treatments which can be found in the excellent monograph by Allen and Tildesley (1987) and in the review of NEMD by the present

authors (Evans and Morriss, 1984a).

Consider the potential energy, Φ , of a system of N interacting particles. The potential energy can always be expanded into a sum of pair, triplet, ... interactions:

$$\Phi(r) = \frac{1}{2!} \sum \phi^{(2)}(\mathbf{r}_i, \mathbf{r}_j) + \frac{1}{3!} \sum \phi^{(3)}(\mathbf{r}_i, \mathbf{r}_j, \mathbf{r}_k) + \dots \quad (6.1.3)$$

For the inert gas fluids it is known that the the total potential energy can be reasonably accurately written as a sum of effective pair interactions with an effective pair interaction potential denoted $\phi(\mathbf{r}_i, \mathbf{r}_j)$. The Lennard-Jones potential, ϕ^{LJ} , is frequently used as an effective pair potential,

$$\phi^{\text{LJ}}(\mathbf{r}_i, \mathbf{r}_j) = \phi^{\text{LJ}}(r_{ij}) \equiv 4\epsilon \left[\left(\frac{\sigma}{r_{ij}} \right)^{12} - \left(\frac{\sigma}{r_{ij}} \right)^6 \right] \quad (6.1.4)$$

The potential energy of the two particles i, j is solely a function of their separation distance r_{ij} and is independent of the relative orientation of their separation vector \mathbf{r}_{ij} . The Lennard-Jones potential is characterised by a well depth ϵ , which controls the energy of the interaction, and a distance σ , which is the distance at which the potential energy of the pair changes sign due to the cancellation of the Van der Waals attractive forces by the short ranged quantum repulsive forces. If $\epsilon/k_B = 119.8\text{K}$ and $\sigma = 3.405\text{\AA}$, the Lennard-Jones potential forms a surprisingly accurate representation of liquid argon (Hansen and Verlet, 1969). For proper scaling during simulations, all calculations are performed in reduced units where $\epsilon/k_B = \sigma = m = 1$. This amounts to measuring all distances in units of σ , all temperatures in units of ϵ/k_B and all masses in units of m . The Lennard-Jones potential is often truncated at a distance, $r_c = 2.5\sigma$. Other potentials that are commonly used include the Weeks-Chandler-Andersen potential, usually written as WCA, which is the Lennard-Jones potential truncated at the position of minimum potential energy ($2^{1/6}\sigma$) and then shifted up so that the potential is zero at the cutoff.

$$\begin{aligned} \phi^{\text{WCA}}(r_{ij}) &= 4\epsilon \left[\left(\frac{\sigma}{r_{ij}} \right)^{12} - \left(\frac{\sigma}{r_{ij}} \right)^6 \right] + \epsilon, & r_{ij} < 2^{1/6}\sigma \\ &= 0, & r_{ij} > 2^{1/6}\sigma \end{aligned} \quad (6.1.5)$$

The main advantage of this potential is its extremely short range of interaction. This permits simulations to be carried out much more quickly than is possible with the longer ranged Lennard-Jones potential. Another short ranged potential than is often used is the soft sphere potential which omits the r^{-6} term from the Lennard-Jones potential. The soft sphere potential is often truncated at 1.5σ .

In molecular dynamics one simply solves the equations of motion for a system of ($N \sim 100 - 100000$) interacting particles. The force on particle i , due to particle j , \mathbf{F}_{ij} , is evaluated from

the equation,

$$\mathbf{F}_{ij} = - \frac{\partial \phi_{ij}}{\partial \mathbf{r}_i} \quad (6.1.6)$$

The N interacting particles are placed in a cubic cell which is surrounded by an infinite array of identical cells - so-called periodic boundary conditions. To compute the force on a given particle in the primitive cell one locates the closest (or minimum) image positions of the other $N-1$ particles. The minimum image of particle i , may be within the primitive cell, or in one of the surrounding image cells (see Figure 6.1). One then finds all the minimum images particles for i , that lie within the potential cutoff distance r_c and uses (6.1.6) to compute the contributions to the force on i , $\mathbf{F}_i = \sum \mathbf{F}_{ij}$.

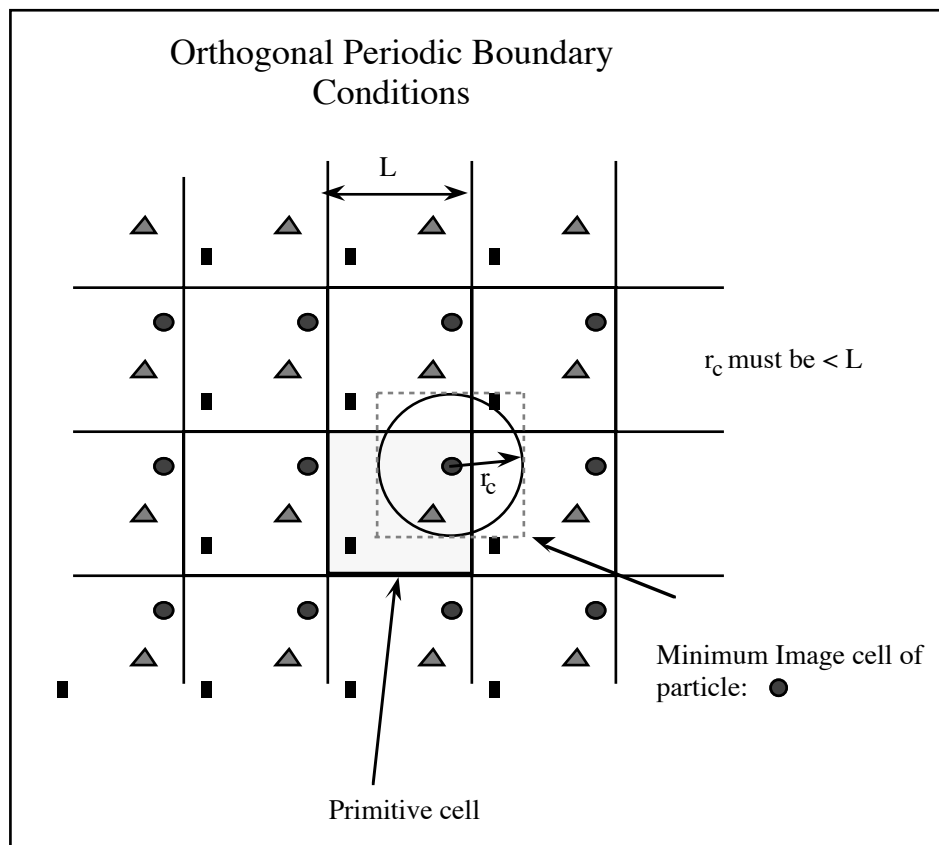


Figure 6.1.

Finally one solves Newton's or Hamilton's equations of motion for the system

$$\begin{aligned} \dot{\mathbf{r}}_i &= \frac{\mathbf{p}_i}{m} \\ \dot{\mathbf{p}}_i &= \mathbf{F}_i \end{aligned} \quad (6.1.7)$$

If, during the course of the motion, particle i leaves the primitive cell it will be replaced under the periodic boundary condition convention by an image of itself, travelling with exactly the same

momentum, one lattice vector distant. We prefer to use Hamilton's form for the equations of motion because this form is much more convenient than the Newtonian form both for NEMD and for equilibrium molecular dynamics with velocity dependent forces (such as thermostats). We often solve these equations of motion using a 5th order Gear predictor-corrector method. In studies of the transient response of systems to external fields we use the less efficient Runge-Kutta methods. Unlike the Gear algorithms, Runge-Kutta methods are self-starting, achieving full accuracy in the first timestep.

We will now give a summary of some of the synthetic NEMD algorithms that have been used to calculate Navier-Stokes transport coefficients.

6.2 Self Diffusion

The first NEMD algorithm for self-diffusion was devised by Holian (Erpenbeck and Wood, 1977). In this elegant scheme the self-diffusion coefficient was evaluated as the limiting value of the mutual diffusion coefficient as the two species become identical. In this limit the two species differ only by a colour label which plays no role in their subsequent dynamics but which is reset in a probabilistic fashion as particles cross a labelling plane. A concentration gradient in coloured species is set up and the mutual diffusion coefficient is calculated from the constitutive relation (colour current/colour gradient). If the labels or colours of the atoms are ignored, the simulation is an ordinary equilibrium molecular dynamics simulation. If one calculates the species density as a function of position, the periodic boundary conditions imply that it is a periodic *saw tooth* profile. Exactly how sharp the teeth are, is not clear. The technique is inhomogeneous and is not applicable to mutual diffusion of species which are really different molecules. If the species are really distinct, the relabelling process will obviously generate discontinuities in pressure and energy.

The techniques we will describe are homogeneous. They do not create concentration gradients or coupled temperature gradients as does the Holian scheme. The algorithms can be extended to calculate mutual diffusion or thermal diffusion coefficients of actual mixtures (MacGowan and Evans, 1986a and Evans and MacGowan, 1987).

We begin by considering the Green-Kubo relation for the self diffusion coefficient (§4.1):

$$D = \int_0^{\infty} dt \langle v_{xi}(t) v_{xi}(0) \rangle \quad (6.2.1)$$

We design a Hamiltonian so that the susceptibility of the colour current to the magnitude of the perturbing colour field is closely related to the single-particle velocity autocorrelation function (6.2.1). Consider the *colour Hamiltonian* (Evans et. al., 1983)

$$H = H_0 - \sum_{i=1}^N c_i x_i F(t), \quad t > 0 \quad (6.2.2)$$

where H_0 is the unperturbed Hamiltonian. The c_i are called colour charges. We call this property colour rather than charge to emphasise that H_0 is independent of the set of colour charges $\{c_i\}$. At equilibrium, in the absence of the colour field, the dynamics is colour blind. For simplicity we consider an even number of particles N , with

$$c_i = (-1)^i. \quad (6.2.3)$$

The response we consider is the colour current density J_x ,

$$J_x = \frac{1}{V} \sum_{i=1}^N c_i \dot{x}_i \quad (6.2.4)$$

Since we are dealing with a Hamiltonian system, AIF (§5.3), is automatically satisfied. The dissipation function is

$$\dot{H}_0^{\text{ad}} = F(t) \sum_{i=1}^N c_i v_{xi} = F(t) J_x V \quad (6.2.5)$$

Linear response theory therefore predicts that (§5.1 & §5.3),

$$\langle J_x(t) \rangle = \beta V \int_0^t ds \langle J_x(t-s) J_x(0) \rangle_0 F(s) \quad (6.2.6)$$

where the propagator implicit in $J_x(t-s)$ is the field **free** equilibrium propagator. (Were we considering electrical rather than colour conductivity, equation (6.2.6) would give the Kubo expression for the electrical conductivity.) To obtain the diffusion coefficient we need to relate the colour current autocorrelation function to the single particle velocity autocorrelation function. This relation, as we shall see, depends slightly on the choice of the equilibrium ensemble. If we choose the canonical ensemble then

$$\langle J_x(t) J_x(0) \rangle_c = \frac{1}{V^2} \sum_{i,j} c_i c_j \langle v_{xi}(t) v_{xj}(0) \rangle_c \quad (6.2.7)$$

In the thermodynamic limit, for the canonical ensemble, if $j \neq i$, then $\langle v_{xi}(t) v_{xj}(0) \rangle = 0$, $\forall t$. This is clear since if c is the sound speed, $v_{xj}(0)$ can only be correlated with other particles within its *sound cone* (ie a volume with radius, ct). In the thermodynamic limit there will always be infinitely more particles outside the sound cone than within it. Since the particles outside this cone cannot possibly be correlated with particle i , we find that,

$$\langle J_x(t) J_x(0) \rangle_c = \frac{1}{V^2} \sum_{i=1}^N c_i^2 \langle v_{xi}(t) v_{xi}(0) \rangle_c = \frac{N}{V^2} \langle v_x(t) v_x(0) \rangle_c \quad (6.2.8)$$

Combining this equation with the Green-Kubo relation for self diffusion gives,

$$D = \frac{1}{\beta \rho} \lim_{t \rightarrow \infty} \lim_{F \rightarrow 0} \frac{\langle J_x(t) \rangle}{F} \quad (6.2.9)$$

If we are working within the *molecular dynamics* ensemble in which the total linear momentum of the system is zero, then v_{xi} is not independent of v_{xj} . In this case there is an order N^{-1} correction to this equation and the self diffusion coefficient becomes (Evans et. al., 1983),

$$D = \frac{N-1}{N} \frac{1}{\beta\rho} \lim_{t \rightarrow \infty} \lim_{F \rightarrow 0} \frac{\langle J_x(t) \rangle}{F} \quad (6.2.10)$$

In the absence of a thermostat the order of the limits in (6.2.9,10) is important. They cannot be reversed. If a thermostat is applied to the system a trivial application of the results of §5.3 allows the limits to be taken in either order.

As an example of the use of thermostats we will now derive the Gaussian isokinetic version of the colour diffusion algorithm. Intuitively it is easy to see that as the heating effect is nonlinear (that is $O(F^2)$), it does not effect the linear response. The equations of motion we employ are:

$$\dot{\mathbf{q}}_i = \frac{\mathbf{p}_i}{m} \quad (6.2.11)$$

and

$$\dot{\mathbf{p}}_i = \mathbf{F}_i + \mathbf{ic}_i F - \alpha(\mathbf{p}_i - \mathbf{mic}_i J_x / n) \quad (6.2.12)$$

where the Gaussian multiplier required to thermostat the system is obtained from the constraint equation

$$\frac{1}{m} \sum_{i=1}^N (\mathbf{p}_i - \mathbf{mic}_i J_x / n)^2 = 3Nk_B T \quad (6.2.13)$$

In this definition of the temperature we calculate the peculiar particle velocities relative to the streaming velocity of **each species**. If one imagined that the two species are physically separated, then this definition of the temperature is independent of the bulk velocity of the two species. In the absence of this definition of the peculiar kinetic energy, the thermostat and the colour field would work against each other and the temperature would have an explicit quadratic dependence on the colour current. Combining (6.1.12 & 13) we identify the thermostating multiplier as

$$\alpha = \frac{\sum m \mathbf{F}_i \cdot (\mathbf{p}_i - \mathbf{mic}_i J_x / n)}{\sum \mathbf{p}_i \cdot (\mathbf{p}_i - \mathbf{mic}_i J_x / n)} \quad (6.2.14)$$

In the original paper, (Evans, et.al., 1983), the thermostat was only applied to the components of the velocity which were orthogonal to the colour field. It can be shown that the **linear** response of these two systems is identical, provided the systems are at the same state point (in particular if the systems have the same temperature).

The algorithm is homogeneous since if we translate particle i and its interacting neighbours, the total force on i remains unchanged. The algorithm is also consistent with ordinary periodic boundary conditions (Figure 6.1). There is no change in the colour charge of particles if they enter or leave the primitive cell. It may seem paradoxical that we can measure diffusion coefficients without the presence of concentration gradients, however we have replaced the chemical potential gradient which drives real diffusion with a fictitious colour field. A gradient in chemical potential implies a composition gradient and a coupled temperature gradient. Our colour field acts homogeneously and leads to no temperature or density gradients. Linear response theory, when applied to our fictitious colour field, tells us how the transport properties of our fictitious mechanical system relate to the thermal transport process of diffusion.

By applying a sinusoidal colour field $F(t) = F_0 e^{i\omega t}$, we can calculate the entire equilibrium velocity autocorrelation function. Noting the amplitude and the relative phase of the colour current we can calculate the complex frequency dependent susceptibility

$$\chi(\omega) = \int_0^{\infty} dt e^{-i\omega t} \chi(t) = - \lim_{F \rightarrow 0} \frac{J(\omega)}{F(\omega)} \quad (6.2.15)$$

An inverse Fourier-Laplace transform gives of $\chi(t)$ gives the velocity autocorrelation function.

Figure 6.2 shows the results of computer simulations of the diffusion coefficient for the 108 particle Lennard-Jones fluid at a reduced temperature of 1.08 and a reduced density of 0.85. The open circles were obtained using the algorithm outlined in this section (Evans et. al., 1983) which is based on equation (6.2.10). We see the colour conductivity (left y-axis) and the diffusion coefficient (right y-axis), plotted as a function of the colour current. The self diffusion coefficient is obtained by extrapolating the current to zero. The arrow denoted 'EMD', shows the results of equilibrium molecular dynamics where the diffusion coefficient was obtained (Levesque and Verlet, 1970), by integrating the velocity autocorrelation function (§4.1). The nonequilibrium and nonequilibrium simulations are in statistical agreement with each other.

Also shown in Figure 6.2, are the results of simulations performed at constant colour current, rather than constant applied colour field. We will return to this matter when we describe Norton ensemble methods in §6.6.

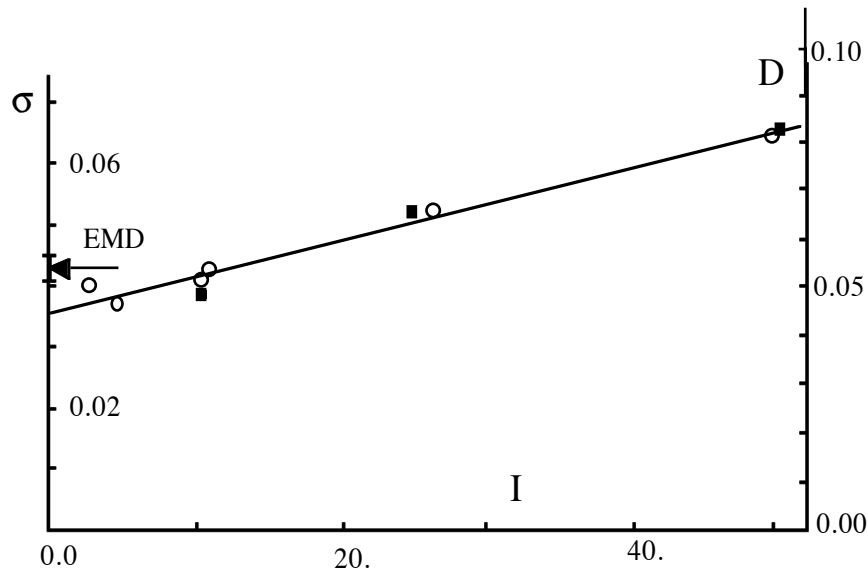


Figure 6.2

The filled in squares are the results of nonequilibrium simulations which were performed at constant colour current rather than constant applied colour field. The constant current methods will be described in more detail in §6.8. Briefly, one treats the colour field $F(t)$ as a Lagrange multiplier whose value is chosen in such a way that the colour current is a constant of the motion. It is clear from the diagram that the constant current and constant colour field simulations are also in statistical agreement with each other.

In terms of computational efficiency, the self diffusion coefficient, being a single particle property, is far more efficiently computed from equilibrium simulations rather than from the algorithm given above. The algorithm we have outlined above is useful for pedagogical reasons. It is the simplest NEMD algorithm. It is also the basis for developing algorithms for the mutual diffusion coefficients of mixtures (Evans and MacGowan, 1987). The mutual diffusion coefficient, being a collective transport property, is difficult to calculate using equilibrium molecular dynamics (Erpenbeck, 1989). If the two coloured species are distinct electrically charged species, the colour conductivity is actually the electrical conductivity and the algorithm given above provides a simple means for its calculation.

6.3 Couette Flow and Shear Viscosity

We now describe a homogeneous algorithm for calculating the shear viscosity. Among the Navier-Stokes transport processes, shear viscosity is unique in that a steady, homogeneous, algorithm is possible using only the periodic boundary conditions to drive the system to a nonequilibrium state. Apart from the possible presence of a thermostat, the equations of motion can be simple Newtonian equations of motion. We will begin by describing how to adapt periodic boundary conditions for planar Couette flow. We will assume that the reader is familiar with the use of fixed orthogonal periodic boundary conditions in equilibrium molecular dynamics simulations (Allen and Tildesley, 1987). Because shearing periodic boundaries alone can be used to drive shear flow, an understanding of the so-called *Lees and Edwards boundary conditions* (Lees and Edwards, 1972) is sufficient to define an algorithm for planar Couette flow. This algorithm is called the *Boundary Driven* algorithm. As this algorithm is based simply on the adaptation of periodic boundary conditions to simulations of shear flow, the algorithm is exact arbitrarily far from equilibrium.

From a theoretical point of view the Boundary Driven algorithm is difficult to work with. Because there is no explicit external field appearing in the equations of motion one cannot employ response theory to link the results obtained from these simulations with say, the Green-Kubo relations for shear viscosity. From a numerical point of view this algorithm also has some disadvantages. This will lead us to a discussion of the so-called SLLOD algorithm. This algorithm still employs Lees-Edwards boundary conditions but it eliminates all of the disadvantages of the simple boundary driven method. The SLLOD algorithm is also exact arbitrarily far from equilibrium.

Lees Edwards Shearing Periodic Boundaries

Figure 6.3 shows one way of representing planar Couette flow in a periodic system. In the Figure we only employ 2 particles per unit cell. In an actual computer simulation this number typically ranges from about one hundred to possibly several tens of thousands. As the particles move under Newton's equations of motion they feel the interatomic forces exerted by the particles within the unit cell and by the image particles whose positions are determined by the instantaneous lattice vectors of the periodic array of cells. The motion of the image cells defines the strain rate, $\gamma \equiv \partial u_x / \partial y$, for the flow. The motion of the cell images is such that their individual origins move with an x-velocity which is proportional to the y-coordinate of the particular cell origin.

$$\mathbf{u}(\mathbf{r}, t) = \mathbf{i} \gamma y \tag{6.3.1}$$

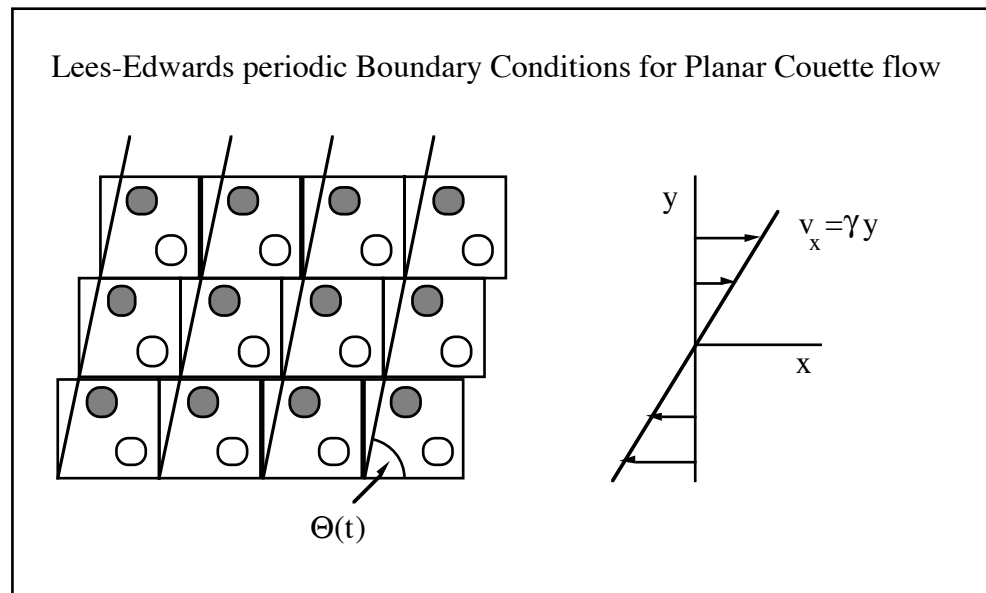


Figure 6.3

If the Reynolds number is sufficiently small and turbulence does not occur, we expect that the motion of image particles above and below any given cell will, **in time**, induce a linear streaming velocity $\mathbf{u}(\mathbf{r})$, on each of the particles within the cell.

If during the course of time, a given particle moves out of a cell it will be replaced by its periodic image. If the particle moves through a y -face of a cell (that is, through the planes $y=0$ or $y=L$) the replacing image particle will not have the same laboratory velocity, nor necessarily the same x -coordinate. This movement of particles into and out of the primitive cell promotes the generation of a stable linear streaming velocity profile.

Although there are jump discontinuities in both the laboratory coordinates and the laboratory velocities of particles between cells there is no way in which the particles can actually sense the boundaries of any given cell. They are merely bookkeeping devices. The system is spatially homogeneous. As we shall see those components of particle velocity and position which are discontinuous have **NO** thermodynamic meaning.

We have depicted the Lees Edwards boundary conditions in the so-called *sliding brick* representation. There is a completely equivalent *deforming cube* representation that one can use if one prefers (see Figure 6.4). We will mainly use the language of the sliding brick representation - our choice is completely arbitrary however.

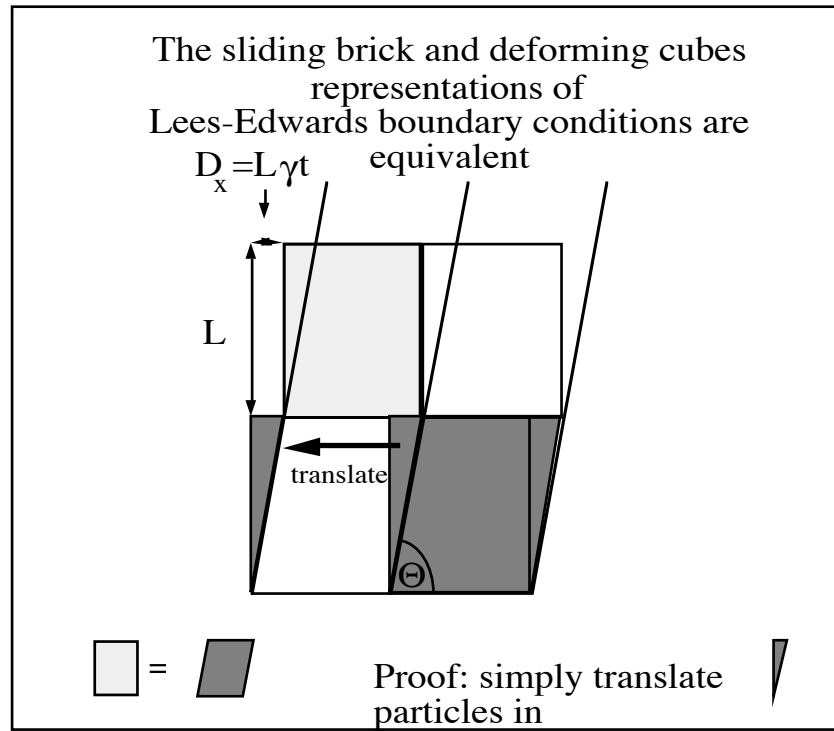


Figure 6.4

We will now consider the motion of particles under Lees Edwards boundary conditions in more detail. Consider a simulation cube of side L , located so that the streaming velocity at the cube origin is zero (that is the cube $0 < \{x,y,z\} < L$). The laboratory velocity of a particle i is then the sum of two parts; a peculiar or thermal velocity \mathbf{c}_i , and a streaming velocity $\mathbf{u}(\mathbf{r}_i)$, so

$$\dot{\mathbf{r}}_i = \mathbf{c}_i + \mathbf{u}(\mathbf{r}_i) \quad (6.3.2)$$

Imagine that at $t = 0$ we have the usual periodic replication of the simulation cube where the boundary condition is

$$\mathbf{r}_i = (\mathbf{r}_i)_{\text{mod } L} \quad (6.3.3)$$

(with the modulus of a vector defined to be the vector of the moduli of the elements). As the streaming velocity is a function of y only, we need to consider explicitly boundary crossings in the y direction. At $t = 0$, \mathbf{r}_i has images at \mathbf{r}_i' at $\mathbf{r}_i + \mathbf{j}L$, and \mathbf{r}_i'' at $\mathbf{r}_i - \mathbf{j}L$. After time t the positions of particle i and these two images are given by

$$\begin{aligned} \mathbf{r}_i(t) &= \mathbf{r}_i(0) + \int_0^t ds \dot{\mathbf{r}}_i(s) = \mathbf{r}_i(0) + \int_0^t ds (\mathbf{c}_i + \mathbf{i} \gamma y_i) \\ \mathbf{r}_i'(t) &= \mathbf{r}_i'(0) + \int_0^t ds (\mathbf{c}_i' + \mathbf{i} \gamma y_i') \end{aligned} \quad (6.3.4)$$

$$\mathbf{r}_i''(t) = \mathbf{r}_i''(0) + \int_0^t ds (\mathbf{c}_i'' + \mathbf{i} \gamma y_i'')$$

where \mathbf{c}_i and y_i (and their images) are functions of time. Now by definition the peculiar velocities of a particle and all of its periodic images are equal, $\mathbf{c}_i = \mathbf{c}_i' = \mathbf{c}_i''$, so that

$$\begin{aligned} \mathbf{r}_i'(t) &= \mathbf{r}_i(0) + \mathbf{j}L + \int_0^t ds (\mathbf{c}_i + \mathbf{i} \gamma (y_i + L)) \\ &= \mathbf{r}_i(0) + \int_0^t ds (\mathbf{c}_i + \mathbf{i} \gamma y_i) + \mathbf{j}L + \mathbf{i} \gamma L t \\ &= \mathbf{r}_i(t) + \mathbf{j}L + \mathbf{i} \gamma L t \end{aligned} \quad (6.3.5)$$

Similarly we can show that

$$\mathbf{r}_i''(t) = \mathbf{r}_i(t) - \mathbf{j}L - \mathbf{i} \gamma L t \quad (6.3.6)$$

If $\mathbf{r}_i(t)$ moves out the bottom of the simulation cube, it is replaced by the image particle at $\mathbf{r}_i'(t)$

$$\mathbf{r}_i^{\text{new}} = (\mathbf{r}_i')_{\text{mod } L} = (\mathbf{r}_i + \mathbf{i} \gamma L t)_{\text{mod } L} \quad (6.3.7)$$

or if $\mathbf{r}_i(t)$ moves out of the top of the simulation cube, it is replaced by the image particle at $\mathbf{r}_i''(t)$

$$\mathbf{r}_i^{\text{new}} = (\mathbf{r}_i'')_{\text{mod } L} = (\mathbf{r}_i - \mathbf{i} \gamma L t)_{\text{mod } L} \quad (6.3.8)$$

The change in the laboratory velocity of a particle is given by the time derivative of equations (6.3.7) and (6.3.8). These rules for imaging particles and their velocities are shown schematically in Figure 6.4.

There is a major difficulty with the boundary driven algorithm. The way in which the boundaries induce a shearing motion to the particles takes time to occur, approximately given by the sound traversal time for the primitive cell. This is the minimum time taken for the particles to realise that the shear is taking place. The boundary driven method as described above, therefore **cannot** be used to study time dependent flows. The most elegant solution to this problem introduces the SLLOD algorithm. We will defer a discussion of thermostats and the evaluation of thermodynamic properties until after we have discussed the SLLOD algorithm.

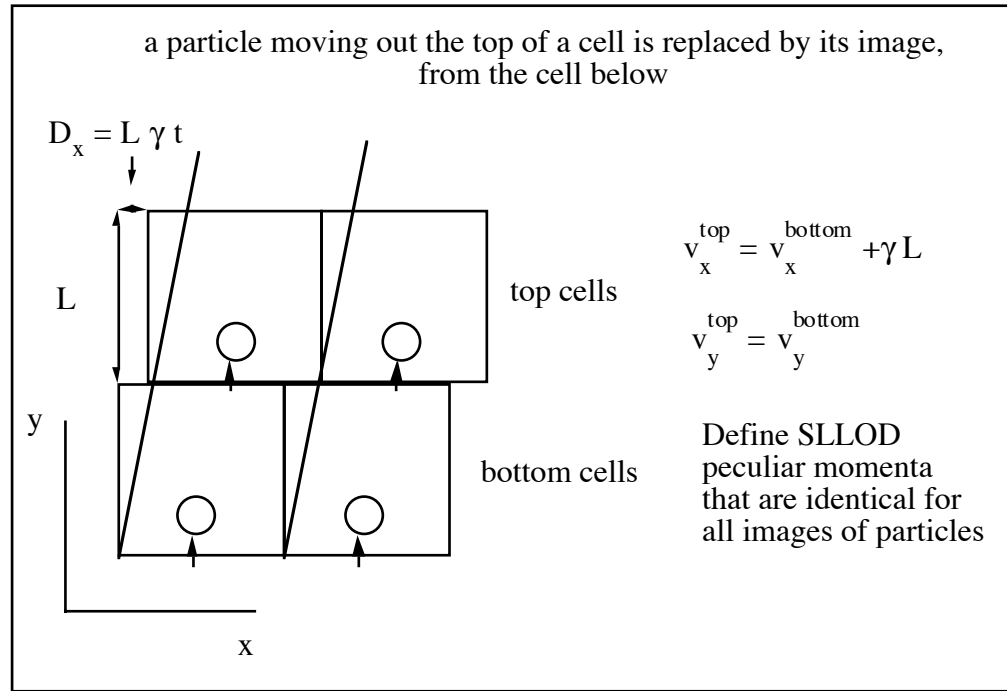


Figure 6.5

The SLLOD Algorithm

The Boundary Driven shear flow algorithm has a number of disadvantages, the principle one being its lack of contact with response theory. We will now describe two synthetic field algorithms for simulating any form of flow deformation. Historically the first fictitious force method proposed for viscous flow calculations was the DOLLS tensor method (Hoover et.al, 1980). This method can be derived from the DOLLS tensor Hamiltonian,

$$H = H_0 + \sum_{i=1}^N \mathbf{q}_i \mathbf{p}_i : (\nabla \mathbf{u}(t))^T \quad (6.3.9)$$

It generates the following equations of motion

$$\begin{aligned} \dot{\mathbf{q}}_i &= \frac{\mathbf{p}_i}{m} + \mathbf{q}_i \cdot \nabla \mathbf{u} \\ \dot{\mathbf{p}}_i &= \mathbf{F}_i - \nabla \mathbf{u} \cdot \mathbf{p}_i \end{aligned} \quad (6.3.10)$$

These equations of motion **must** be implemented with compatible periodic boundary conditions. If the strain rate tensor has only one nonzero element and it is off-diagonal, the deformation is planar Couette flow and Lees-Edwards boundary conditions must be used. If the strain rate tensor is isotropic then the flow is dilational and the appropriate variation of Lees-Edwards boundaries must be used. Other flow geometries can also be simulated using these equations.

One can see from the first of the equations (6.3.10), that since $d\mathbf{q}_i/dt$ is obviously a laboratory velocity, the momenta \mathbf{p}_i are *peculiar* with respect to the low Reynolds number streaming velocity $\mathbf{u}(\mathbf{r}) = \mathbf{r} \cdot \nabla \mathbf{u}$. We call this streaming velocity profile the zero wavevector profile. If the Reynolds number is sufficiently high for turbulence to occur, the \mathbf{p}_i are peculiar only with respect to the zero wavevector profile. They will not be peculiar with respect to any possible turbulent velocity profiles.

From (6.3.10) the dissipation is easily shown to be

$$\dot{H}_0^{\text{ad}} = -\nabla \mathbf{u} : \mathbf{P} \mathbf{V} \quad (6.3.11)$$

where \mathbf{P} is the instantaneous pressure tensor (3.8.19), whose kinetic component is given in terms of the peculiar momenta \mathbf{p}_i . Since the DOLLS tensor equations of motion are derivable from a Hamiltonian, the $\text{AI}\Gamma$ condition is clearly satisfied and we see immediately from equations (6.3.11) and (5.3.8), that in the linear regime, close to equilibrium, the shear and bulk viscosities will be related to equilibrium fluctuations via the Green-Kubo formula (T.6.3). This **proves** that the DOLLS tensor algorithm is correct for the limiting linear regime. The linear response of the pressure tensor is therefore,

$$\langle \mathbf{P}(t) \rangle = -\beta V \int_0^t ds \langle \mathbf{P}(t-s) \mathbf{P} \rangle : \nabla \mathbf{u} \quad (6.3.12)$$

The DOLLS tensor method has now been replaced by the SLLOD algorithm (Evans and Morriss, 1984b). The only difference between the SLLOD algorithm and the DOLLS tensor equations of motion involves the equation of motion for the momenta. The Cartesian components that couple to the strain rate tensor are transposed. Unlike the DOLLS tensor equations, the SLLOD equations of motion **cannot** be derived from a Hamiltonian.

$$\begin{aligned} \dot{\mathbf{q}}_i &= \frac{\mathbf{p}_i}{m} + \mathbf{q}_i \cdot \nabla \mathbf{u} \\ \dot{\mathbf{p}}_i &= \mathbf{F}_i - \mathbf{p}_i \cdot \nabla \mathbf{u} \end{aligned} \quad (6.3.13)$$

It is easy to see that the dissipation function for the SLLOD algorithm is precisely the same as for the DOLLS tensor equations of motion. In spite of the absence of a generating Hamiltonian, the SLLOD equations also satisfy $\text{AI}\Gamma$. This means that the linear response for both systems is identical and is given by (6.3.12). By taking the limit $\gamma \rightarrow 0$, followed by the limit $t \rightarrow \infty$, we see that the linear shear viscosity can be calculated from a nonequilibrium simulation, evolving under either the SLLOD or the DOLLS tensor equations of motion. With, $\nabla \mathbf{u} = \mathbf{j}\mathbf{i}(\partial u_x / \partial y)$, and calculating the ratio of stress to strain rate we calculate,

$$\eta = \lim_{t \rightarrow \infty} \lim_{\gamma \rightarrow 0} \frac{-\langle P_{xy}(t) \rangle}{\gamma} \quad (6.3.14)$$

From (6.3.13) we see that the susceptibility is precisely the Green-Kubo expression for the shear viscosity (Table 6.1). Because the linear response of the SLLOD and DOLLS tensor algorithms are related to equilibrium fluctuations by the Green-Kubo relations, these algorithms can be used to calculate the reaction of systems to time-varying strain rates. If the shear rate is a sinusoidal function of time, then the Fourier transform of the susceptibility gives the complex, frequency-dependent shear viscosity measured in viscoelasticity (§2.4 & §4.3).

If the strain rate tensor is isotropic then the equations of motion describe adiabatic dilation of the system. If this dilation rate is sinusoidal then the limiting small field bulk viscosity can be calculated by monitoring the amplitude and phase of the pressure response and extrapolating both the amplitude and frequency to zero (Hoover et.al.1980). It is again easy to see from (6.3.13) that the susceptibility for the dilation induced pressure change, is precisely the Green-Kubo transform of the time dependent equilibrium fluctuations in the hydrostatic pressure (Table 6.1).

Although the DOLLS tensor and SLLOD algorithms have the same dissipation and give the correct **linear** behaviour, the DOLLS tensor algorithm begins to yield incorrect results at quadratic order in the strain rate. These errors show up first as errors in the normal stress differences. For irrotational flows ($\nabla \mathbf{u} = (\nabla \mathbf{u})^T$) so the SLLOD and DOLLS tensor methods are identical, as can easily be seen from their equations of motion.

We will now show that the SLLOD algorithm gives an exact description of shear flow **arbitrarily far from equilibrium**. This method is also correct in the high Reynolds number regime in which laminar flow is unstable. Consider superimposing a linear velocity profile on a canonical ensemble of N-particle systems. This will generate the *local equilibrium* distribution function for Couette flow, f_1

$$f_1 = \frac{\exp[-\beta[\sum m(v_i + i\gamma y_i)^2 / 2 + \Phi]]}{\int d\Gamma \exp[-\beta[\sum m(v_i + i\gamma y_i)^2 / 2 + \Phi]]} \quad (6.3.15)$$

Macroscopically such an ensemble is described by a linear streaming velocity profile,

$$\mathbf{u}(\mathbf{r}, t) = \mathbf{i} \gamma y \quad (6.3.16)$$

so that the second rank strain rate tensor, $\nabla \mathbf{u}$, has only one nonzero element, $(\nabla \mathbf{u})_{yx} = \gamma$. The local equilibrium distribution function is **not** the same as the steady state distribution. This is easily seen when we realise that the shear stress evaluated for f_1 , is zero. The local distribution function is no more than a canonical distribution with a superimposed linear velocity profile. No molecular relaxation has yet taken place.

If we allow this relaxation to take place by advancing time using Newton's equations (possibly supplemented with a thermostat) the system will go on shearing forever. This is because the linear velocity profile of the local distribution generates a **zero** wavevector transverse momentum current. As we saw in § 3.8, the zero wavevector momentum densities is conserved. The transverse momentum current will persist forever, at least for an infinite system.

Now let us see what happens under the SLLOD equations of motion (6.3.12), when the strain rate tensor is given by (6.3.16). Differentiating the first equation, then substituting for $d\mathbf{p}_i/dt$ using the second equation gives,

$$m \ddot{\mathbf{q}}_i = \mathbf{F}_i - \mathbf{i} \gamma p_{yi} + \mathbf{i} (\gamma p_{yi} + m \dot{\gamma} y_i) = \mathbf{F}_i + \mathbf{i} m \dot{\gamma} y_i \quad (6.3.17)$$

If the strain rate γ is switched on at time zero, and remains steady thereafter,

$$\gamma(t) = \gamma \Theta(t) \Rightarrow \dot{\gamma} = \gamma \delta(t) \quad (6.3.18)$$

Thus $d\gamma/dt$ is a delta function at $t=0$. Now consider subjecting a canonical ensemble to these transformed SLLOD equations of motion, (6.3.17). If we integrate the velocity of particle i , over an infinitesimal time interval about zero. We see that,

$$\mathbf{v}_i(0^+) - \mathbf{v}_i(0) = \int_0^{0^+} ds \mathbf{v}(s) = \mathbf{i} \gamma y_i \quad (6.3.19)$$

So at time 0^+ the x -velocity of every particle is incremented by an amount proportional to the product of the strain rate times its y coordinate. At time 0^+ , the other components of the velocity and positions of the particles are unaltered because there are no delta function singularities in their equations of motion. Applying (6.3.19) to a canonical ensemble of systems will clearly generate the local equilibrium distribution for planar Couette flow.

The application of SLLOD dynamics to the canonical ensemble is thus seen to be equivalent to applying Newton's equations to the local distribution function. The SLLOD equations of motion have therefore succeeded in transforming the boundary condition expressed in the form of the local distribution function into the form of a smooth mechanical force which appears as a **mechanical** perturbation in the equations of motion. This property is unique to SLLOD dynamics. It is not satisfied by the DOLLS tensor equations of motion for example. Since one cannot really call into question, the validity of the application of Newtonian dynamics to the local distribution as a correct description of Couette flow we are lead to the conclusion that the adiabatic application of SLLOD dynamics to the canonical ensemble gives an exact description of Couette flow.

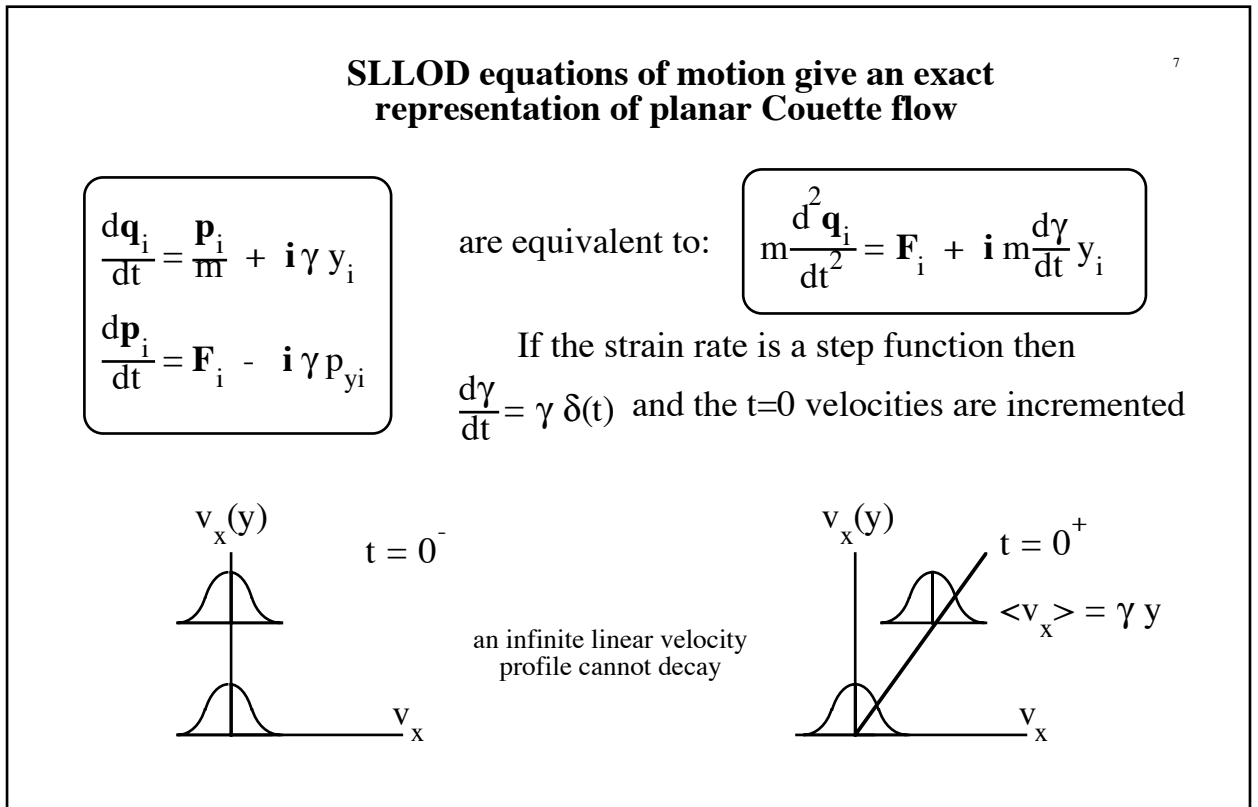


Figure 6.6

Knowing that the SLLOD equations are exact, and that they generate Green-Kubo expressions for the shear and bulk viscosities, provides a **proof** of the validity of the Green-Kubo expressions themselves. The SLLOD transformation of a thermal transport process into a mechanical one, provides us with a direct route to the Green-Kubo relations for the viscosity coefficients. From equation (6.3.13) we see that we already have these relations for both the shear and bulk viscosity coefficients. We also see that these expressions are identical to those we derived in Chapter 4, using the generalised Langevin equation. It is clear that the present derivation is simpler and gives greater physical insight into the processes involved.

Compared to the boundary driven methods, the advantages of using the SLLOD algorithm in computer simulations are many. Under periodic boundaries the SLLOD momenta which are peculiar with respect to the zero wavevector velocity field, and are continuous functions of time and space. This is not so for the laboratory velocities \mathbf{v}_i . The internal energy and the pressure tensor of the system are more simply expressed in terms of SLLOD momenta rather than laboratory momenta. The internal energy E is given as,

$$E(T, \rho, N, \gamma) = \langle H_0 \rangle = \left\langle \sum_{i=1}^N \frac{\mathbf{P}_i^2}{2m} + \frac{1}{2} \sum_{i,j} \phi_{ij} \right\rangle \quad (6.3.21)$$

while the ensemble averaged pressure tensor is,

$$\mathbf{P}(T,\rho,N,\gamma)V = \left\langle \sum_{i=1}^N \frac{\mathbf{p}_i \mathbf{p}_i}{m} - \frac{1}{2} \sum_{i,j} \mathbf{r}_{ij} \cdot \mathbf{F}_{ij} \right\rangle \quad (6.3.21)$$

For simulations of viscoelasticity special measures have to be taken in the boundary driven algorithm to ensure that the time varying strain rate is actually what you expect it to be. In the SLLOD method no special techniques are required for simulations of time dependent flows. One simply has to solve the equations of motion with a time dependent strain rate and ensure that the periodic boundary conditions are precisely consistent with the strain derived by integrating the imposed strain rate $\gamma(t)$.

Since the SLLOD momenta are peculiar with respect to the zero wavevector velocity profile, the obvious way of thermostating the algorithm is to use the equations,

$$\begin{aligned} \dot{\mathbf{q}}_i &= \frac{\mathbf{p}_i}{m} + \mathbf{i} \gamma y_i \\ \dot{\mathbf{p}}_i &= \mathbf{F}_i - \mathbf{i} \gamma p_{yi} - \alpha \mathbf{p}_i \end{aligned} \quad (6.3.22)$$

The thermostating multiplier α , is calculated in the usual way by ensuring that $d(\sum p_i^2)/dt=0$.

$$\alpha = \frac{\sum (\mathbf{F}_i \cdot \mathbf{p}_i - \gamma p_{xi} p_{yi})}{\sum p_i^2} \quad (6.3.23)$$

The temperature is assumed to be related to the peculiar kinetic energy. These equations **assume** that a linear velocity profile is stable. However as we have mentioned a number of times the linear velocity profile is only stable at low Reynolds number, ($Re=\rho m \gamma L^2/\eta$).

In Figure 6.7 we show the shear viscosity of 2048 WCA particles as a function of strain rate. The fluid is close to the Lennard-Jones triple point. The reduced temperature and density are 0.722 and 0.8442 respectively. The simulations were carried out using the Gaussian isokinetic SLLOD algorithm. We see that there is a substantial change in the viscosity with shear rate. Evidently WCA fluids are shear thinning in that the viscosity decreases with increasing strain rate. It turns out that this is common to all simple fluids for all thermodynamic state points. Shear thinning is also a widely observed phenomenon in the rheology of complex molecular fluids.

The imposed shear causes a major change in the microscopic fluid structure. This is manifest in **all** the thermodynamic properties of the system changing with shear rate. In Figure 6.8 we see the internal energy of the fluid plotted as a function of strain rate. For reduced strain rates in the range 0 - 1.5, we see that both the shear viscosity and the internal energy change by approximately 50% compared to their equilibrium values. Furthermore the viscosity coefficient appears to vary as the square root of the strain rate while the energy appears to change with the 1.5 power of the strain rate. Over the range of strain rates studied, the maximum deviation from the

functional forms is 2.5% for the viscosity, and 0.1% for the internal energy. There has been much recent discussion of the relation of these apparently non-analytic dependences to mode-coupling theory (see, Yamada and Kawasaki, 1973; Kawasaki and Gunton, 1973; Ernst et. al., 1978; Evans, 1983; Kirkpatrick, 1984, van Beijeren, 1984 and deSchepper et. al., 1986). It is clear that the final resolution of this matter is still a long way off.

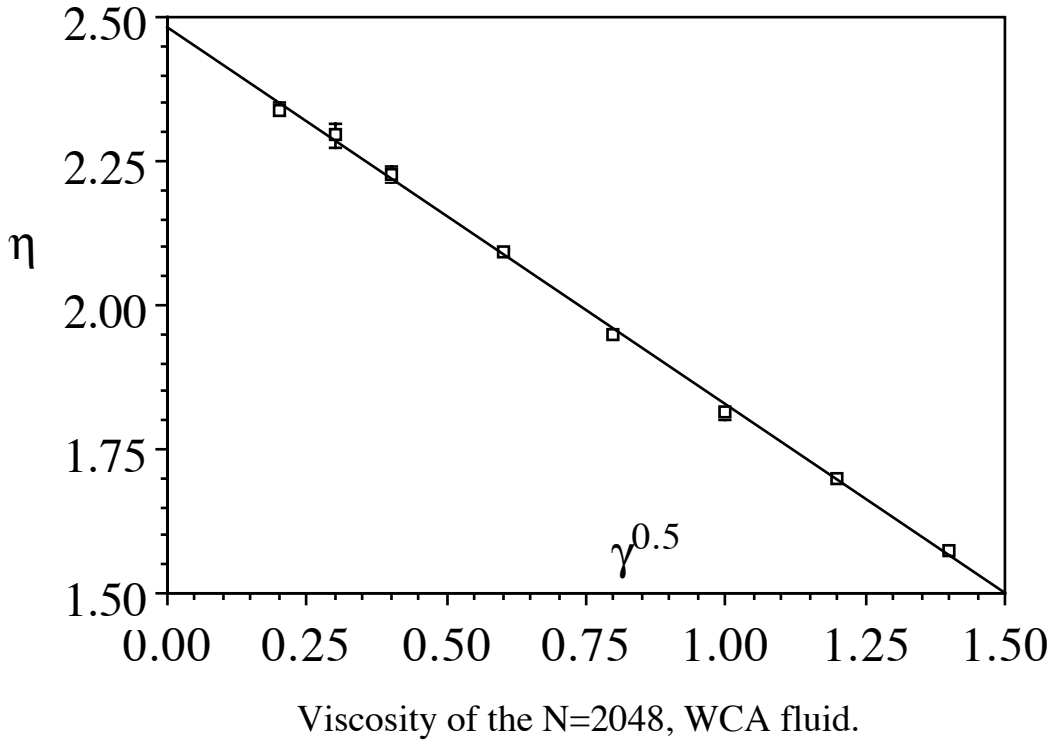


Figure 6.7

One of the most interesting and subtle rheological effects concerns the diagonal elements of the pressure tensor. For Newtonian fluids (ie fluids characterised by a strain rate independent and frequency independent viscosity) the diagonal elements are equal to each other and to their equilibrium values. Far from equilibrium, this is not true. We define normal stress coefficients, η_0 , η_- , (the so-called out-of-plane and in-plane normal stress coefficients) as,

$$\eta_0 \equiv -[P_{zz} - 1/2(P_{xx} + P_{yy})] / 2\gamma \quad (6.3.24)$$

$$\eta_- \equiv -(P_{xx} - P_{yy}) / 2\gamma \quad (6.3.25)$$

Figure 6.9 shows how these coefficients vary as a function of $\gamma^{0.5}$ for the WCA fluid. The out-of-plane coefficient is far larger than the in-plane coefficient, except at very small strain rates where both coefficients go to zero (ie the fluid becomes Newtonian). These coefficients are very difficult to compute accurately. They require both larger and longer simulations to achieve an accuracy that is comparable to that for the shear viscosity. In terms of the macroscopic hydrodynamics of Non-Newtonian fluids, these normal stress differences are responsible for a wide variety of interesting phenomena (eg the Weissenberg effect see Rainwater et. al. (1985 a,b)).

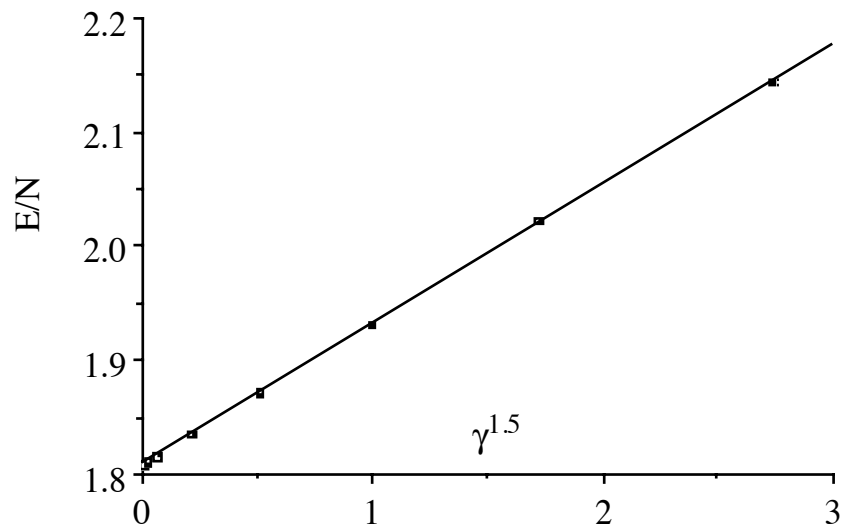
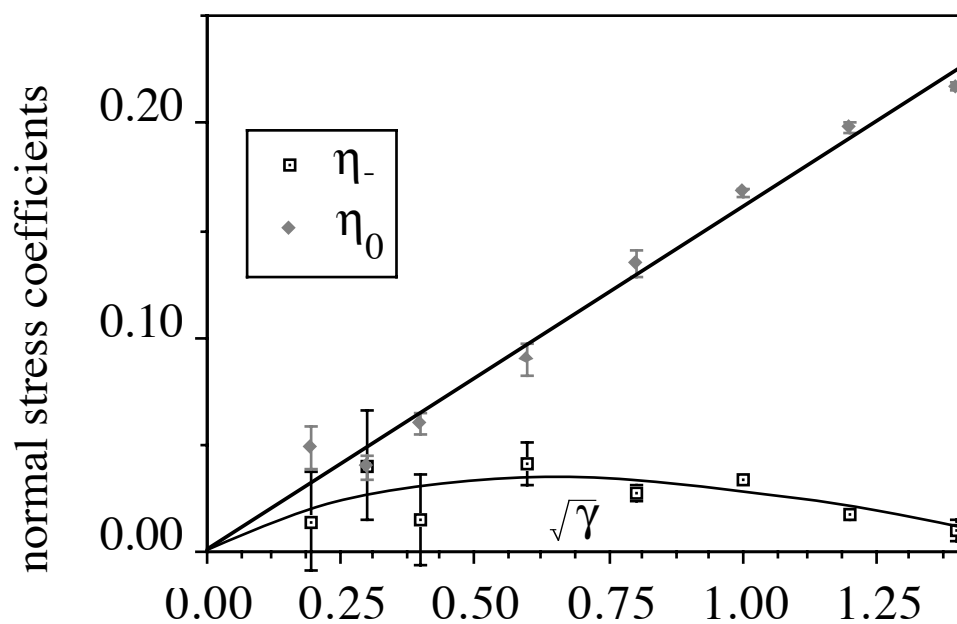


Figure 6.8

If one allows the strain rate to be a sinusoidal function of time and one extrapolates the system response to zero amplitude, one can calculate the linear viscoelastic response of a fluid. Figure 6.10 shows complex frequency dependent shear viscosity for the Lennard-Jones fluid (Evans, 1980), at its triple point.



Normal stress coefficients for the N=2048, WCA fluid.

Figure 6.9

If one compares Figure 6.10 with the Maxwell model for viscoelasticity, Figure 2.4, one sees a qualitative similarity with the low frequency response being viscous and the high frequency response being elastic. The shape of the two sets of curves is however quite different. This is particularly so at low frequencies. An analysis of the low frequency data shows that it is consistent with a nonanalytic square root dependence upon frequency.

$$\tilde{\eta}_R(\omega) = \eta(0) - \eta_{\omega 1} \omega^{0.5} + O(\omega) \quad (6.3.26)$$

$$\tilde{\eta}_I(\omega) = \eta_{\omega 1} \omega^{0.5} + O(\omega)$$

In (6.3.26) η_R , η_I , are the real and imaginary parts of the viscosity coefficient. Since the frequency dependent viscosity is the Fourier-Laplace transform of the memory function (2.4.12), we can use the Tauberian theorems (Doetsch, 1961), to show that if (6.3.26) represents the asymptotic low frequency behaviour of the frequency dependent viscosity, then the memory function must have the form,

$$\lim_{t \rightarrow \infty} \eta(t) = \frac{\eta_{\omega 1} t^{-\frac{3}{2}}}{\sqrt{2\pi}} \quad (6.3.27)$$

This time dependence is again consistent with the time dependence predicted by mode-coupling theory (Pomeau and Resibois, 1975). However as was the case for the strain rate dependence the amplitude of the effect shown in Figure 6.10, is orders of magnitude larger than theoretical predictions. This matter is also the subject of much current research and investigation.

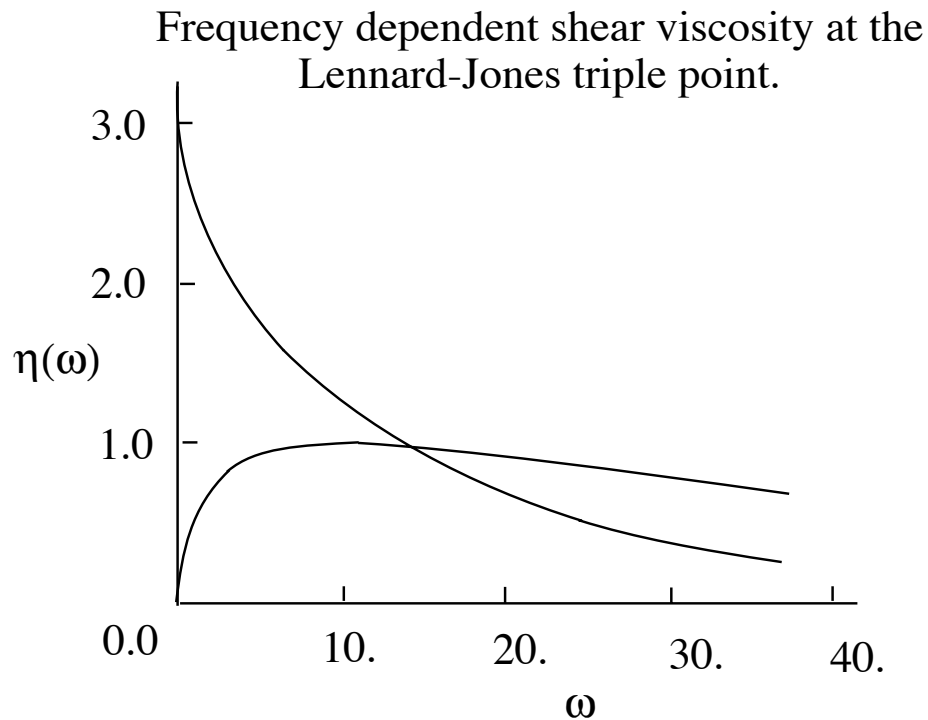


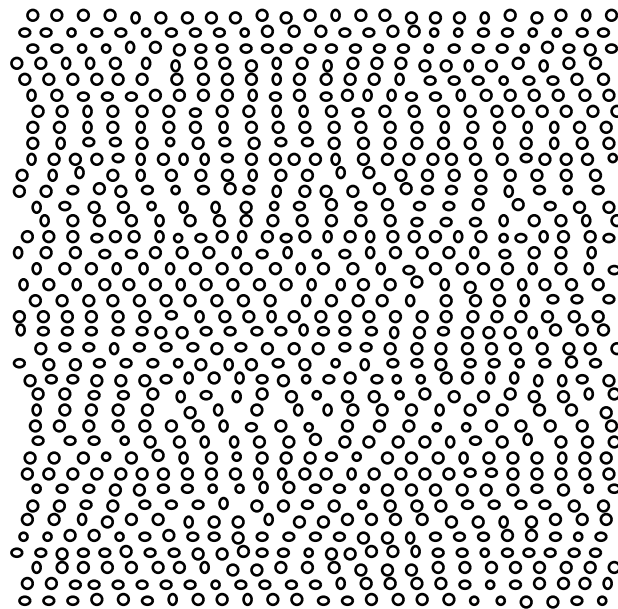
Figure 6.10

Similar *enhanced* long time tails have been observed subsequently in Green-Kubo calculations for the shear viscosity (Erpenbeck and Wood, 1981). Whatever the final explanation for these enhanced long time tails, they are a ubiquitous feature of viscous processes at high densities. They have been observed in the wavevector dependent viscosity (Evans, 1982a) and in

shear flow of 4-dimensional fluids (Evans, 1984). The situation for two dimensional liquids is apparently even more complex (Evans and Morriss 1983a and Morriss and Evans 1989).

6.4 Thermostatting shear flows.

While performing NEMD simulations of thermostatted shear flow for hard-sphere fluids, Erpenbeck (1984) observed that at very high shear rates, fluid particles organised themselves into strings. This was an early observation of a nonequilibrium phase transition. This organisation of particles into strings reduces the rate at which entropy is produced in the system by the external field. This effect is in competition with the kink instability of the strings themselves. If the strings move too slowly across the simulation cell, thermal fluctuations in the curvature of the strings lead to their destruction. A snapshot of a string phase is shown in Figure 6.11. The velocity gradient is vertical and the streaming velocity is horizontal. The system is 896 soft discs at a state point close to freezing and a reduced shear rate of 17.



High shear rate string phase in soft disks

Figure 6.11

The string phase is in fact, stabilised by the use of a thermostat which **assumes** that a linear velocity profile, (implicit in equation (6.3.22)), is stable. Thermostats which make some assumption about the form of the streaming velocity profile are called Profile Biased Thermostats (PBT). All the thermostats we have met so far are Profile Biased. At equilibrium there can be little cause for worry, the streaming velocity must be zero. Away from equilibrium we must be more careful.

Any kink instability that might develop in Erpenbeck's strings, leading to their breakup, would necessarily lead to the formation of large scale *eddies* in the streaming velocity of the fluid. The Profile Biased Thermostat would interpret any incipient eddy motion as *heat*, and then thermostat would try to *cool* the system by suppressing the eddy formation. This in effect

stabilises the string phase (Evans and Morriss,1986).

Thermostats for streaming or convecting flows - PUT

Profile Biased Thermostats for shear flow assume that the kinetic temperature T_B , for a system undergoing planar Couette flow can be defined from the equation,

$$dNk_B T_B = \left\langle \sum_{i=1}^N m (\mathbf{v}_i - \mathbf{i}\gamma y_i)^2 \right\rangle. \quad (6.4.1)$$

In this equation d is the number of dimensions and N is the number of particles. The term $\mathbf{i}\gamma y_i$ is the *presumed* streaming velocity at the location of particle i . Once the form of the streaming velocity profile is established it is a simple matter to use peculiar velocity scaling, Gaussian isokinetic or Nosé methods to thermostat the shearing system.

At small shear rates and low Reynolds number, the Lees-Edwards shearing periodic boundary conditions do indeed lead to a planar velocity profile of the form assumed in (6.4.1). In Erpenbeck's (1984) simulations the Reynolds numbers, ($Re = \rho m \gamma L^2 / \eta$), were very large (10^3 - 10^5). The assumption of a linear streaming velocity profile under these conditions is extremely dubious. Suppose that at high Reynolds number the linear velocity profile assumed in (6.4.1) is not stable. In a freely shearing system with Lees-Edwards geometry, this might manifest itself in an S-shaped kink developing in the velocity profile. If (6.3.22) is used to maintain the temperature, the thermostat will interpret the development of this secondary flow as a component of the temperature. This increase in temperature will be continuously removed by the thermostat, leading to a damping of the secondary flow.

If we rewrite the SLLOD equations in terms of laboratory momenta,

$$\dot{\mathbf{r}}_i = \frac{\mathbf{p}_i}{m}, \quad \dot{\mathbf{p}}_i = \mathbf{F}_i - \alpha \left(\frac{\mathbf{p}_i}{m} - \mathbf{i}\gamma y_i \right) \quad (6.4.2)$$

then the momentum current, \mathbf{J} ,

$$\mathbf{J}(\mathbf{r}, t) \equiv \rho(\mathbf{r}, t) \mathbf{u}(\mathbf{r}, t) = \sum \mathbf{p}_i \delta(\mathbf{r}_i(t) - \mathbf{r}) \quad (6.4.3)$$

satisfies the following continuity equation,

$$\begin{aligned} \frac{\partial \mathbf{J}}{\partial t} &= -\nabla \cdot (\mathbf{P} + \rho \mathbf{u} \mathbf{u}) - \alpha \sum_{i=1}^n \left(\frac{\mathbf{p}_i}{m} - \mathbf{i}\gamma y_i \right) \delta(\mathbf{r}_i - \mathbf{r}) \\ &= -\nabla \cdot (\mathbf{P} + \rho \mathbf{u} \mathbf{u}) - \frac{\alpha}{m} (\mathbf{J}(\mathbf{r}, t) - \rho(\mathbf{r}, t) \mathbf{u}_{\text{linear}}(\mathbf{r}, t)) \end{aligned} \quad (6.4.4)$$

The derivation of this equation is carried out by a simple supplementation of the Irving-Kirkwood procedure (§3.7,8). We have to add the contribution of the thermostat to equation (3.7.7 - 15). Comparing equation (6.4.4) with the momentum conservation equation (2.1.12) we see that the thermostat could exert a stress on the system. The expected divergence terms ($\rho \mathbf{u}\mathbf{u} + \mathbf{P}$), are present on the right hand side of (6.4.4). However the term involving α , the thermostating term, is new and represents the force exerted on the fluid by the thermostat. It will only vanish if a linear velocity profile is *stable* and,

$$\mathbf{J}(\mathbf{r},t) = \rho(\mathbf{r},t) \mathbf{u}(\mathbf{r},t) = \mathbf{i} m \gamma \nabla \mathbf{r}. \quad (6.4.5)$$

At high Reynolds number this condition might not be true. For simulations at high Reynolds numbers one needs a thermostat which makes no assumptions whatever about the form of the streaming velocity profile. The thermostat should not even assume that a stable profile exists. These ideas led to development (Evans and Morriss, 1986), of Profile Unbiased Thermostats (PUT).

The PUT thermostat begins by letting the simulation itself define the local streaming velocity $\mathbf{u}(\mathbf{r},t)$. This is easily done by replacing the delta functions in (6.4.3) by microscopically small cells in the simulation programme. The temperature of a particular cell at \mathbf{r} , $T(\mathbf{r},t)$, can be determined from the equation,

$$\frac{dn(\mathbf{r},t) - d}{2} k_B T(\mathbf{r},t) \equiv \sum \frac{m}{2} (\mathbf{v}_i - \mathbf{u}(\mathbf{r},t))^2 \delta(\mathbf{r}_i(t) - \mathbf{r}) \quad (6.4.6)$$

where $n(\mathbf{r},t)$ is the number density at \mathbf{r},t (the delta function has unit volume). The number of degrees of freedom in the cell is $dn(\mathbf{r},t) - d$, because d degrees of freedom are used to determine the streaming velocity of the cell.

The PUT thermostatted SLLOD equations of motion can be written as,

$$\frac{d\mathbf{r}_i}{dt} = \frac{\mathbf{p}_i}{m}, \quad \frac{d\mathbf{p}_i}{dt} = \mathbf{F}_i - \alpha \left(\frac{\mathbf{p}_i}{m} - \mathbf{u}(\mathbf{r},t) \right) \delta(\mathbf{r}_i - \mathbf{r}) \quad (6.4.7)$$

The streaming velocity, $\mathbf{u}(\mathbf{r},t)$, is not known in advanced but is computed as time progresses from its definition, (6.4.3). The thermostat multiplier α , could be a Gaussian multiplier chosen to fix the peculiar kinetic energy (6.4.6). Equally well the multiplier could be a Nosé-Hoover multiplier. The momentum equation for the PUT thermostatted system reads,

$$\begin{aligned} \frac{d\mathbf{J}}{dt} &= -\nabla \cdot (\mathbf{P} + \rho \mathbf{u}\mathbf{u}) - \alpha \sum \left(\frac{\mathbf{p}_i}{m} - \mathbf{u}(\mathbf{r},t) \right) \delta(\mathbf{r}_i - \mathbf{r}) \\ &= -\nabla \cdot (\mathbf{P} + \rho \mathbf{u}\mathbf{u}) - \frac{\alpha}{m} (\mathbf{J}(\mathbf{r},t) - \rho(\mathbf{r},t) \mathbf{u}(\mathbf{r},t)) \end{aligned} \quad (6.4.8)$$

From the definition of the streaming velocity of a cell we know that, $n(\mathbf{r},t)\mathbf{u}(\mathbf{r},t) = \sum \mathbf{p}_i/m \delta(\mathbf{r}_i(t) - \mathbf{r})$. We also know that, $n(\mathbf{r},t)\mathbf{u}(\mathbf{r},t) = \sum \mathbf{u}(\mathbf{r},t) \delta(\mathbf{r}_i(t) - \mathbf{r}) = \mathbf{u}(\mathbf{r},t) \sum \delta(\mathbf{r}_i(t) - \mathbf{r})$. Thus the thermostating term in (6.4.8), vanishes for all values of \mathbf{r} .

In terms of practical implementation in computer programmes, PUT thermostats can only be used in simulations involving large numbers of particles. Thus far their use has been restricted to simulations of two dimensional systems. At low Reynolds numbers where no strings are observed in Profile Biased simulations, it is found that Profile Unbiased simulations yield results for all properties which are indistinguishable from those computed using PBT methods. However at high strain rates the results obtained using the two different thermostating methods are quite different. No one has observed a string phase while using a PUT thermostat.

6.5 Thermal Conductivity

Thermal conductivity has proven to be one of the most difficult transport coefficients to calculate. Green-Kubo calculations are notoriously difficult to perform. Natural NEMD where one might simulate heat flow between walls maintained at different temperatures (Tenenbaum, Ciccotti & Gallico [1982]) is also fraught with major difficulties. Molecules stack against the walls leading to a major change in the microscopic fluid structure. This means that the results can be quite different from those characteristic of the bulk fluid. In order to measure a statistically significant heat flux, one must use enormously large temperature gradients. These gradients are so large that the absolute temperature of the system may change by 50% in a few tens of Ångstroms. The thermal conductivity that one obtains from such simulations is an average over the wide range of temperatures and densities present in the simulation cell.

We will now describe the most efficient presently known algorithm for calculating the thermal conductivity, (Evans, 1982b). This technique is synthetic, in that a fictitious field replaces the temperature gradient as the force driving the heat flux. Unlike real heat flow, this technique is homogeneous with no temperature or density gradients. We start with the Green-Kubo expression for the thermal conductivity (§4.4),

$$\lambda = \frac{V}{k_B T^2} \int_0^{\infty} dt \langle J_{Q_z}(t) J_{Q_z}(0) \rangle \quad (6.5.1)$$

where J_{Q_z} is the z component of the heat flux vector. It appears to be impossible to construct a Hamiltonian algorithm for the calculation of thermal conductivity. This is because the equations of motion so obtained are discontinuous when used in conjunction with periodic boundary conditions. We shall instead invent an external field and its coupling to the phase of the N-particle system so that the heat flux generated by this external field is trivially related to the magnitude of the heat flux induced by a real temperature gradient.

Aided by the realisation that the heat flux vector is the diffusive energy flux, computed in a co-moving coordinate frame (see equation 3.8.18), we proposed the following equations of motion,

$$\dot{\mathbf{q}}_i = \frac{\mathbf{p}_i}{m} \quad (6.5.2)$$

$$\dot{\mathbf{p}}_i = \mathbf{F}_i + (E_i - \bar{E}) \mathbf{F}(t) - \frac{1}{2} \sum_{j=1}^N \mathbf{F}_{ij} (\mathbf{q}_{ij} \cdot \mathbf{F}(t)) + \frac{1}{2N} \sum_{j,k}^N \mathbf{F}_{jk} (\mathbf{q}_{jk} \cdot \mathbf{F}(t)) \quad (6.5.3)$$

where E_i is the energy of particle i and,

$$\bar{E} = \frac{1}{N} \left\{ \sum_{i=1}^N \frac{\mathbf{p}_i^2}{2m} + \frac{1}{2} \sum_{i \neq j} \phi_{ij} \right\}, \quad (6.5.4)$$

the **instantaneous** average energy per particle.

There is no known Hamiltonian which generates these equations but they do satisfy AIF. This means that linear response theory can be applied in a straightforward fashion. The equations of motion are momentum preserving, homogeneous and compatible with the usual periodic boundary conditions. It is clear from the term $(E_i - \bar{E}) \mathbf{F}(t)$ that these equations of motion will drive a heat current. A particle whose energy is greater than the average energy will experience a force in the direction of \mathbf{F} , while a particle whose energy is lower than the average will experience a force in the $-\mathbf{F}$ direction. *Hotter* particles are driven with the field; *colder* particles are driven against the field.

If the total momentum is zero it will be conserved and the dissipation is

$$\dot{H}_0^{\text{ad}} = \mathbf{F}(t) \cdot \left\{ \sum_{i=1}^N \frac{\mathbf{p}_i E_i}{m} - \frac{1}{2} \sum_{i,j} \mathbf{q}_{ij} \left(\frac{\mathbf{p}_i \cdot \mathbf{F}_{ij}}{m} \right) \right\} = \mathbf{F}(t) \cdot \mathbf{J}_Q V \quad (6.5.5)$$

Using linear response theory we have

$$\langle \mathbf{J}_Q(t) \rangle = -\beta V \int_0^t ds \langle \mathbf{J}_Q(t-s) \mathbf{J}_Q \rangle \cdot \mathbf{F}(s) \quad (6.5.6)$$

Consider a field $\mathbf{F}=(0,0,F_z)$, then taking the limit $t \rightarrow \infty$ we find that the ratio of the induced heat flux to the product of the absolute temperature and the magnitude of the external field is in fact the thermal conductivity.

$$\lambda = \frac{V}{k_B T^2} \int_0^\infty dt \langle J_{Q_z}(t) J_{Q_z}(0) \rangle = \lim_{F \rightarrow 0} \frac{-\langle J_{Q_z}(\infty) \rangle}{T F}. \quad (6.5.7)$$

In the linear limit the effect the heat field has on the system is identical to that of a logarithmic temperature gradient ($F = \partial \ln T / \partial z$). The theoretical justification for this algorithm is tied to **linear** response theory. No meaning is known for the finite field susceptibility.

In 1983 Gillan and Dixon introduced a slightly different synthetic method for computing the thermal conductivity (Gillan and Dixon, 1983). Although their algorithm is considerably more complex to apply in computer simulations, their equations of motion look quite similar to those given above. Gillan's synthetic algorithm is of some theoretical interest since it is the only known

algorithm which violates momentum conservation and AIΓ, (MacGowan and Evans, 1986b).

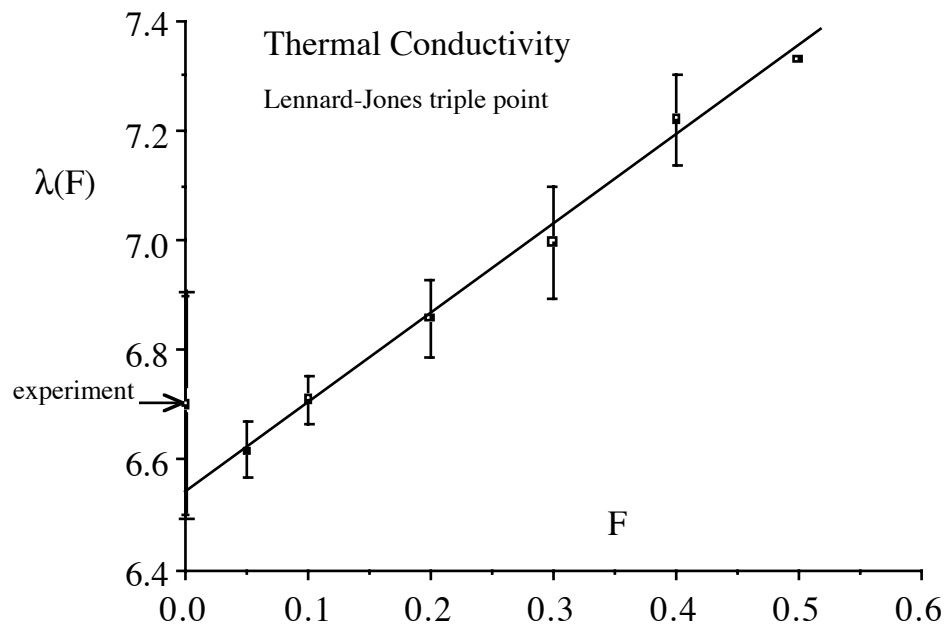



Figure 6.12

Figure 6.12 shows the thermal conductivity of the triple point Lennard-Jones fluid computed as a function of the strength of the heat field. We also show the experimental data for argon assuming that argon can be modelled by the standard Lennard-Jones model ($\epsilon/k_B=119.8K$, $\sigma=3.405\text{\AA}$). The experimental uncertainties are so large that that if we used an accurate potential function, we could calculate the thermal conductivity more accurately than it can be measured. 

6.6 Norton Ensemble Methods

Norton and Thévenin's theorems are of fundamental importance in electrical circuit theory (Brophy, 1966). They prove that any network of resistors and power supplies can be analysed in terms of equivalent circuits which include either ideal current or ideal voltage sources. These two theorems are an example of the macroscopic duality that exists between what are generally recognised as thermodynamic fluxes and thermodynamic forces - in the electrical circuit case, electrical currents and the electromotive force. Indeed in our earlier introduction to linear irreversible thermodynamics (Chapter 2), there was an apparent arbitrariness with respect to our definition of forces and fluxes. At no stage did we give a convincing macroscopic distinction between the two.

Microscopically one might think that there is a clear and unambiguous distinction that can be drawn. For an arbitrary mechanical system subject to a perturbing external field the dissipation can be written as, $dH_0^{ad}/dt \equiv -J(\mathbf{\Gamma})F_e(t)$. The dissipative flux is the phase variable $J(\mathbf{\Gamma})$ and the force is the time dependent independent variable, $F_e(t)$. This might seem to remove the arbitrariness. However, suppose that we complicate matters a little and regard the external field $F_e(t)$, as a Gaussian multiplier in a feedback scheme designed to stop the flux $J(\mathbf{\Gamma})$, from changing. We might wish to perform a constant current simulation. In this case the imposed *external* field $F_e(t)$, is in fact a phase variable, $F_e(\mathbf{\Gamma})$. Even microscopically the distinction between forces and fluxes is more complex than is often thought.

In this section we will explore the statistical mechanical consequences of this duality. Until recently the Green-Kubo relations were only known for the conventional Thévenin ensemble in which the forces are the independent state defining variables. We will derive their Norton ensemble equivalents. We will then show how these ideas have been applied to algorithms for isobaric molecular dynamics simulations. This work will provide the necessary background for the derivations, in Chapter 9, of fluctuation expressions for the derived properties of nonequilibrium steady states including the nonlinear inverse Burnett coefficients.

Gaussian Constant Colour Current Algorithm

From the colour Hamiltonian (6.2.2) we see that the equations of motion for colour conductivity in the Thévenin ensemble are,

$$\begin{aligned}\dot{\mathbf{q}}_i &= \frac{\mathbf{p}_i}{m} \\ \dot{\mathbf{p}}_i &= \mathbf{F}_i + c_i \mathbf{F}(t).\end{aligned}\tag{6.6.1}$$

These equations are the adiabatic version of (6.2.11 & 12). We will now treat the colour field as a Gaussian multiplier chosen to fix the colour current and introduce a thermostat.

Our first step is to redefine the momenta (Evans and Morriss, 1985), so that they are measured with respect to the species current of the particles. Consider the following set of equations of motion

$$\dot{\mathbf{q}}_i = \frac{\mathbf{p}_i}{m} + \frac{c_i \mathbf{I}(t)}{\sum_{i=1}^N c_i^2} \quad (6.6.2)$$

$$\dot{\mathbf{p}}_i = \mathbf{F}_i - c_i \boldsymbol{\lambda} - \alpha \mathbf{p}_i$$

where α is the thermostating multiplier and $\boldsymbol{\lambda}$ is the current multiplier. These equations are easily seen to be equivalent to (6.2.11 & 12). We distinguish two types of current, a canonical current \mathbf{J} defined in terms of the canonical momenta,

$$\mathbf{J} \equiv \sum \frac{c_i \mathbf{P}_i}{m} \quad (6.6.3)$$

and a kinetic current \mathbf{I} , where

$$\mathbf{I} \equiv \sum c_i \dot{\mathbf{q}}_i \quad (6.6.4)$$

We choose $\boldsymbol{\lambda}$ so that the canonical current is always zero, and α so that the canonical (ie. peculiar) kinetic energy is fixed. Our constraint equations are therefore,

$$\mathfrak{g}_d = \sum \frac{c_i \mathbf{P}_i}{m} - \mathbf{J} = 0 \quad (6.6.5)$$

and

$$\mathfrak{g}_T = \frac{1}{m} \sum \mathbf{p}_i^2 - 3Nk_B T = 0 \quad (6.6.6)$$

The Gaussian multipliers may be evaluated in the usual way by summing moments of the equations of motion and eliminating the accelerations using the differential forms of the constraints. We find that

$$\boldsymbol{\lambda} = \frac{\sum c_i \mathbf{F}_i}{\sum c_i^2} \quad (6.6.7)$$

and

$$\alpha = \frac{\sum \mathbf{F}_i \cdot \mathbf{p}_i}{\sum \mathbf{p}_i^2} \quad (6.6.8)$$

If we compare the Gaussian equations of motion with the corresponding Hamiltonian equations we see that the Gaussian multiplier λ can be identified as a fluctuating external colour field which maintains a constant colour current. It is however, a phase variable. Gauss' principle has enabled us to go from a constant field nonequilibrium ensemble to the conjugate ensemble where the current is fixed. The Gaussian multiplier fluctuates in the precise manner required to fix the current. The distinction drawn between canonical and kinetic currents has allowed us to decouple the Lagrange multipliers appearing in the equations of motion. Furthermore setting the canonical current to zero is equivalent to setting the kinetic current to the required value \mathbf{I} . This can be seen by taking the charge moment of (6.6.2). If the canonical current is zero then,

$$\sum c_i \dot{\mathbf{q}}_i = \frac{\sum c_i^2 \mathbf{I}(t)}{\sum c_i^2} = \mathbf{I}(t) \quad (6.6.9)$$

In this equation the current, which was formerly a phase variable has now become a possibly time dependent external force.

In order to be able to interpret the response of this system to the external current field, we need to compare the system's equations of motion with a macroscopic constitutive relation. Under adiabatic conditions the second order form of the equations of motion is

$$m \ddot{\mathbf{q}}_i = \mathbf{F}_i + m \dot{\mathbf{I}}(t) \frac{c_i}{\sum c_i^2} - \lambda \mathbf{e}_i \quad (6.6.10)$$

We see that to maintain a constant current $\mathbf{I}(t)$ we must apply a fluctuating colour field \mathbf{E}_{eff} ,

$$\mathbf{E}_{\text{eff}}(t) = \frac{m \dot{\mathbf{I}}(t)}{\sum c_i^2} - \lambda \quad (6.6.11)$$

The adiabatic rate of change of internal energy H_0 is given by

$$\dot{H}_0^{\text{ad}} = - \sum \left[\frac{c_i \mathbf{p}_i \cdot \lambda}{m} + \frac{c_i \mathbf{F}_i \cdot \mathbf{I}}{\sum c_i^2} \right] = -\mathbf{J} \cdot \lambda - \mathbf{I} \cdot \lambda \quad (6.6.12)$$

As the current, $\mathbf{J}=\mathbf{J}(\Gamma)$ is fixed at the value zero, the dissipation is $-\mathbf{I}(t) \cdot \lambda(\Gamma)$. As expected the current is now an external time dependent field while the colour field is a phase variable. Using linear response theory we have

$$\langle \boldsymbol{\lambda}(t) \rangle = \beta \int_0^t ds \langle \boldsymbol{\lambda}(t-s) \boldsymbol{\lambda} \rangle \cdot \mathbf{I}(s) \quad (6.6.13)$$

which gives the linear response result for the phase variable component of the effective field. Combining (6.6.13) with (6.6.11) the effective field is therefore

$$\mathbf{E}_{\text{eff}}(t) = \int_0^t ds \chi(t-s) \mathbf{I}(s) + \frac{m \dot{\mathbf{I}}(t)}{\sum_i c_i^2} \quad (6.6.14)$$

where the susceptibility χ is the equilibrium λ autocorrelation function,

$$\chi(t) \equiv \beta \langle \lambda(t) \lambda(0) \rangle \quad (6.6.15)$$

Fourier-Laplace transforming we obtain the frequency dependent colour resistance,

$$\bar{\mathbf{R}}(\omega) = \tilde{\chi}(\omega) + \frac{i\omega m}{\sum_i c_i^2} \quad (6.6.16)$$

To compare with the usual Green-Kubo relations which have always been derived for conductivities rather than resistances we find,

$$\tilde{\sigma}(\omega) = \frac{1}{V \tilde{\chi}(\omega) + \frac{N i \omega m}{\sum_{i=1}^N c_i^2}} \quad (6.6.17)$$

This equation shows that the Fourier-Laplace transform of $\chi(t)$ is the memory function of the complex frequency dependent conductivity. In the conjugate constant force ensemble the frequency dependent conductivity is related to the current autocorrelation function

$$\sigma(\omega) = \frac{1}{3V k_B T} \int_0^{\infty} dt e^{-i\omega t} \langle \mathbf{J}(t) \cdot \mathbf{J}(0) \rangle_{\mathbf{E}=0} \quad (6.6.18)$$

From equations (6.6.15 - 18) we see that at **zero** frequency the colour conductivity is given by the integral of the Thévenin ensemble current correlation function while the resistance, which is the reciprocal of the conductivity, is given by the integral of the colour field autocorrelation function computed in the Norton ensemble. Thus at zero frequency the integral of the Thévenin ensemble current correlation function is the reciprocal of the integral of the Norton

ensemble field correlation function. Figure 6.2 gave a comparison of Norton and Thévenin algorithms for computing the colour conductivity. The results obtained for the conductivity are ensemble independent - even in the nonlinear regime far from equilibrium.

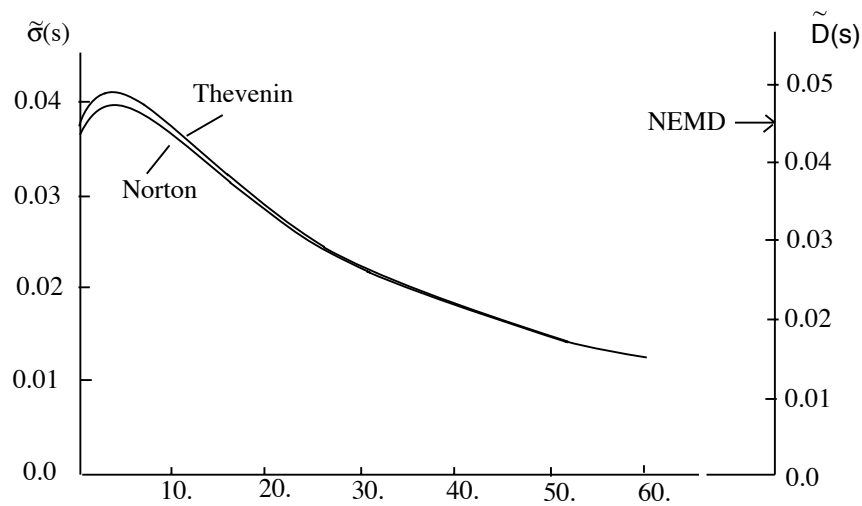


Figure 6.13

The colour conductivity as a function of the Laplace transform variable, s .

In Figure 6.13 we show the reduced colour conductivity plotted as a function of frequency (Evans and Morriss, 1985). The system is identical to the Lennard-Jones system studied in Figure 6.2. The curves were calculated by taking the Laplace transforms of the appropriate equilibrium time correlation functions computed in both the Thévenin and Norton ensembles. Within statistical uncertainties, the results are in agreement. The arrow shows the zero frequency colour conductivity computed using NEMD. The value is taken from Figure 6.2.

6.7 Constant Pressure ensembles

For its first 30 years, molecular dynamics was limited to the microcanonical ensemble. We have already seen how the development of thermostats has enabled simulations to be performed in the isochoric, canonical and isokinetic ensembles. We will now describe molecular dynamics algorithms for performing simulations at constant pressure or constant enthalpy. The technique used to make the pressure rather than the volume, the independent state defining variable, uses essentially the same ideas as those employed in §6.6 to design Norton ensemble algorithms. The methods we describe now are of use for both equilibrium and nonequilibrium simulations.

It is often advantageous, particularly in studies of phase transitions, to work within the isobaric ensemble. It is possible to stabilise the pressure in a number of ways: we will describe the Gaussian method (Evans and Morriss, 1983b) since it was both the first deterministic isobaric technique to be developed and it is conceptually simpler than the corresponding Nosé-Hoover (Hoover, 1985) and Rahman-Parrinello (1980a,b, 1981) schemes. Although it may be slightly more difficult to write the computer programmes, once written they are certainly easier to use. The Gaussian method has the distinct advantage that the pressure is a rigorous constant of the motion whereas the Nosé based schemes (Nosé, 1984) and those of Parrinello and Rahman allow fluctuations in **both** the pressure and the volume.

If one makes a poor initial guess for the density, Nosé-Hoover isobaric algorithms induce sharp density changes in an attempt to correct the density, to that appropriate for the specified mean pressure. Because bulk oscillations damp quite slowly, Nosé-Hoover methods can easily result in the system exploding - a situation that cannot be reversed due to the finite range of the interaction potentials. Gaussian isobaric algorithms are free of these instabilities.

Isothermal-Isobaric molecular dynamics

Consider the SLLOD equations of motion where the strain rate tensor $\nabla \mathbf{u}$ is isotropic . The equations of motion become

$$\dot{\mathbf{q}}_i = \frac{\mathbf{p}_i}{m} + \dot{\boldsymbol{\varepsilon}} \mathbf{q}_i \quad (6.7.1)$$

$$\dot{\mathbf{p}}_i = \mathbf{F}_i - \dot{\boldsymbol{\varepsilon}} \mathbf{p}_i \quad (6.7.2)$$

Now if the system was *cold* ($\mathbf{p}_i=0$ for all i), and non-interacting ($\phi_{ij}=0$), these equations would reduce to

$$\dot{\mathbf{q}}_i = \dot{\varepsilon} \mathbf{q}_i \quad (6.7.3)$$

Since this equation is true for all particles i , it describes a uniform dilation or contraction of the system. This dilation or contraction is the same in each coordinate direction, so if the system initially occupied a cube of volume V , then the volume would satisfy the following equation of motion.

$$\dot{V} = 3 V \dot{\varepsilon} \quad (6.7.4)$$

For *warm*, interacting systems, the equation of motion for \mathbf{q}_i shows that the canonical momentum \mathbf{p}_i is in fact peculiar with respect to the streaming velocity $d\varepsilon/dt$ \mathbf{q}_i . The dissipation for the system (6.7.1&2) is

$$\dot{H}_0 = -\dot{\varepsilon} \sum_{i=1}^N \left\{ \frac{1}{m} \mathbf{p}_i \cdot \mathbf{p}_i + \mathbf{F}_i \cdot \mathbf{q}_i \right\} = -3 p V \dot{\varepsilon} \quad (6.7.5)$$

Since H_0 is the internal energy of the system we can combine (6.7.5) with the equation of motion for the volume to obtain the first law of thermodynamics for adiabatic compression,

$$\dot{H}_0 = -3 p V \dot{\varepsilon} = -p \dot{V} \quad (6.7.6)$$

It is worth noting that these equations are true **instantaneously**. One does not need to employ any ensemble averaging to obtain equation (6.7.6). By choosing the dilation rate $d\varepsilon/dt$ to be a sinusoidal function of time, these equations of motion can be used to calculate the bulk viscosity. Our purposes are however to use the dilation rate as a multiplier to maintain the system at a constant hydrostatic pressure. Before we do this however, we will introduce a Gaussian thermostat into the equations of motion;

$$\dot{\mathbf{q}}_i = \frac{\mathbf{p}_i}{m} + \dot{\varepsilon} \mathbf{q}_i \quad (6.7.7)$$

$$\dot{\mathbf{p}}_i = \mathbf{F}_i - \dot{\varepsilon} \mathbf{p}_i - \alpha \mathbf{p}_i \quad (6.7.8)$$

The form for the thermostat multiplier is determined by the fact that the momenta in (6.7.7&8) are peculiar with respect to the dilating coordinate frame. By taking the moment of (6.7.8) with respect to \mathbf{p}_i , and setting the time derivative of the peculiar kinetic energy to zero we observe that,

$$\alpha = -\dot{\epsilon} + \frac{\sum_{i=1}^N \mathbf{F}_i \cdot \mathbf{p}_i}{\sum_{i=1}^N p_i^2} \quad (6.7.9)$$

Differentiating the product pV , (6.7.5) with respect to time gives,

$$3\dot{p}V + 3p\dot{V} = \sum_{i=1}^N \left\{ \frac{2}{m} \dot{\mathbf{p}}_i \cdot \mathbf{p}_i + \dot{\mathbf{q}}_i \cdot \mathbf{F}_i + \mathbf{q}_i \cdot \frac{\partial \mathbf{F}_i}{\partial \mathbf{q}_i} \cdot \dot{\mathbf{q}}_i + \sum_{j \neq i} \mathbf{q}_i \cdot \frac{\partial \mathbf{F}_i}{\partial \mathbf{q}_j} \cdot \dot{\mathbf{q}}_j \right\} \quad (6.7.10)$$

The first term on the LHS is zero because the pressure is constant, and the first term on the RHS is zero because the peculiar kinetic energy is constant. Substituting the equations of motion for $d\mathbf{q}_i/dt$ and dV/dt , and we can solve for the dilation rate.

$$\dot{\epsilon} = - \frac{\frac{1}{2m} \sum_{i \neq j} \mathbf{q}_{ij} \cdot \mathbf{p}_{ij} (\phi_{ij}'' + \frac{\dot{\phi}_{ij}}{q_{ij}})}{\frac{1}{2} \sum_{i \neq j} q_{ij}^2 (\phi_{ij}'' + \frac{\dot{\phi}_{ij}}{q_{ij}}) + 9pV} \quad (6.7.11)$$

combining this equation with (6.7.9) gives a closed expression for the thermostat multiplier α .

In summary our isothermal/isobaric molecular dynamics algorithm involves solving $6N+1$ first order equations of motion (equations (6.7.4,7&8)). There are two subtleties to be aware of before implementing this method. Firstly the pressure is sensitive to the long range tail of the interaction potential. In order to obtain good pressure stability the long range truncation of the potential needs to be handled carefully. Secondly, if a Gear predictor corrector scheme is used to integrate the equations of motion then some care must be taken in handling the higher order derivatives of the coordinates and momenta under periodic boundary conditions. More details are given in Evans and Morriss (1983b) and (1984a).

Isobaric-isoenthalpic molecular dynamics

For the adiabatic constant pressure equations of motion we have already shown that the first law of thermodynamics for compression is satisfied

$$\dot{H}_0 = -p \dot{V} \quad (6.7.12)$$

It is now easy to construct equations of motion for which the enthalpy $I = H_0 + pV$, is a constant of the motion. The constraint we wish to impose is that

$$\dot{I} = \dot{H}_0 + \dot{p}V + p\dot{V} = 0 \quad (6.7.13)$$

Combining these two equations we see that for our adiabatic constant pressure equations of motion the rate of change of enthalpy is simply

$$\dot{I} = \dot{p}V \quad (6.7.14)$$

This equation says that if our adiabatic equations preserve the pressure then the enthalpy is automatically constant. The isobaric-isoenthalpic equations of motion are simply obtained from the isothermal-isobaric equations by dropping the constant temperature constraint. The isoenthalpic dilation rate can be shown to be (Evans and Morriss, 1984a),

$$\dot{\varepsilon} = \frac{\frac{2}{m} \sum_{i=1}^N \mathbf{p}_i \cdot \mathbf{F}_i - \frac{1}{2m} \sum_{i \neq j} \mathbf{q}_{ij} \cdot \mathbf{p}_{ij} \left(\phi_{ij}'' + \frac{\phi_{ij}'}{q_{ij}} \right)}{\frac{2}{m} \sum_{i=1}^N \mathbf{p}_i^2 + \frac{1}{2} \sum_{i \neq j} q_{ij}^2 \left(\phi_{ij}'' + \frac{\phi_{ij}'}{q_{ij}} \right) + 9pV} \quad (6.7.15)$$

6.8 The Constant Stress ensemble

We will now give another example of the usefulness of the Norton ensemble. Suppose we wish to calculate the yield stress of a Bingham plastic - a solid with a yield stress. If we use the SLLOD method outlined above the Bingham plastic will always yield simply because the strain **rate** is an input into the simulation. It would not be easy to determine the yield stress from such a calculation. For simulating yield phenomena one would prefer the shear stress as the input variable. If this were the case simulations could be run for a series of incremented values of the shear stress. If the stress was less than the yield stress, the solid would strain elastically under the stress. Once the yield stress was exceeded, the material would shear.

Here we discuss a simple method for performing NEMD simulations in the stress ensemble. We will use this as an opportunity to illustrate the use the Nosé-Hoover feedback mechanism. We will also derive linear response expressions for the viscosity within the context of the Norton ensemble. The equations of motion for shear flow, thermostatted using the Nosé-Hoover thermostat are

$$\dot{\mathbf{q}}_i = \frac{\mathbf{p}_i}{m} + \mathbf{n}_x \gamma \mathbf{y}_i \quad (6.8.1)$$

$$\dot{\mathbf{p}}_i = \mathbf{F}_i - \mathbf{n}_x \gamma p_{yi} - \xi \mathbf{p}_i \quad (6.8.2)$$

$$\dot{\xi} = \frac{K(\Gamma) - K_0}{Q_\xi} = \frac{1}{\tau_\xi^2} \left(\frac{K(\Gamma)}{K_0} - 1 \right) \quad (6.8.3)$$

Using the Nosé-Hoover feedback mechanism we relate the rate of change of the strain rate, γ , to the degree to which the instantaneous shear stress, $-P_{xy}(\Gamma)$ differs from a specified mean value, $-S_{xy}(t)$. We therefore determine the strain rate from the differential equation,

$$\dot{\gamma} = \frac{(P_{xy}(\Gamma) - S_{xy}(t)) V}{Q_\gamma} \quad (6.8.4)$$

If the instantaneous stress is greater (ie more negative) than the specified value, the strain rate will decrease in an attempt to make the two stresses more nearly equal. The relaxation constant Q_γ should be chosen so that the timescale for feedback fluctuations is roughly equal to the natural relaxation time of the system.

From the equations of motion, the time derivative of the internal energy $H_0 = \sum_i p_i^2/2m + \Phi$, is easily seen to be,

.

$$H_0 = -P_{xy}V\dot{\gamma} - \xi K \quad (6.8.5)$$

The Nosé constant stress, constant temperature dynamics satisfy a Liouville equation in which phase space behaves as a compressible $6N+2$ dimensional fluid. The equilibrium distribution function is a function of the $3N$ particle coordinates, the $3N$ particle momenta, the thermostating multiplier ξ , and strain rate $\dot{\gamma}$, $f_0 = f_0(\mathbf{\Gamma}, \xi, \dot{\gamma})$. The Liouville equation for this system is then

$$\frac{df_0}{dt} = -f_0 \left(\frac{\partial}{\partial \mathbf{\Gamma}} \cdot \dot{\mathbf{\Gamma}} + \frac{\partial}{\partial \xi} \dot{\xi} + \frac{\partial}{\partial \dot{\gamma}} \dot{\gamma} \right) \quad (6.8.6)$$

Since

$$\dot{\xi} = \dot{\xi}(\mathbf{\Gamma}) \quad \text{and} \quad \dot{\gamma} = \dot{\gamma}(\mathbf{\Gamma}) \quad \text{then} \quad \frac{\partial}{\partial \xi} \dot{\xi} = \frac{\partial}{\partial \dot{\gamma}} \dot{\gamma} = 0 \quad (6.8.7)$$

the phase space compression factor $\Lambda(\mathbf{\Gamma})$ is easily seen to be $-3N\dot{\xi}$. If we consider the time derivative of the extended internal energy $H_0 + 1/2 Q_\xi \dot{\xi}^2 + 1/2 Q_\gamma \dot{\gamma}^2$ we find that

$$\begin{aligned} \frac{d}{dt} \left(H_0 + \frac{1}{2} Q_\gamma \dot{\gamma}^2 + \frac{1}{2} Q_\xi \dot{\xi}^2 \right) &= \dot{H}_0 + Q_\gamma \dot{\gamma} \dot{\gamma} + Q_\xi \dot{\xi} \dot{\xi} \\ &= -P_{xy} V \dot{\gamma} - \xi K + \xi (K - K_0) + (P_{xy} - S_{xy}) V \dot{\gamma} \\ &= -\xi K_0 - S_{xy} V \dot{\gamma}. \end{aligned} \quad (6.8.8)$$

If we consider the situation at equilibrium when the set value of the shear stress, $-S_{xy}(t)$, is zero and $K_0 = 3N/2\beta$, the Liouville equation becomes

$$\frac{df_0}{dt} = \beta \xi K_0 f_0 = -\beta f_0 \frac{d \left(H_0 + \frac{1}{2} Q_\gamma \dot{\gamma}^2 + \frac{1}{2} Q_\xi \dot{\xi}^2 \right)}{dt} \quad (6.8.9)$$

Integrating both sides with respect to time gives the equilibrium distribution function for the constant stress Norton ensemble to be

$$f_0 = \frac{\exp[-\beta(H_0 + \frac{1}{2} Q_\gamma \dot{\gamma}^2 + \frac{1}{2} Q_\xi \dot{\xi}^2)]}{\int d\mathbf{\Gamma} \int d\dot{\gamma} \int d\xi \exp[-\beta(H_0 + \frac{1}{2} Q_\gamma \dot{\gamma}^2 + \frac{1}{2} Q_\xi \dot{\xi}^2)]} \quad (6.8.10)$$

The equilibrium distribution function is thus a generalised canonical distribution, permitting strain rate fluctuations. Indeed the mean square strain rate is

$$\langle \gamma^2 \rangle_{S_{xy}=0} = \frac{1}{\beta Q_\gamma} \quad (6.8.11)$$

so the amplitude of the strain rate fluctuations are controlled by the adjustable constant Q_γ .

We wish to calculate the linear response of an equilibrium ensemble of systems (characterised by the distribution f_0 , at time $t=0$), to an externally imposed time dependent shear stress, $-S_{xy}(t)$. For the Nosé-Hoover feedback mechanism the external field is the mean shear stress, and it appears explicitly in the equations of motion (Hood, Evans and Morriss, 1987). This is in contrast to the more difficult Gaussian case (Brown and Clarke, 1986). For the Gaussian feedback mechanism the numerical value of the constraint variable does not usually appear explicitly in the equations of motion. This is a natural consequence of the differential nature of the Gaussian feedback scheme.

The linear response of an arbitrary phase variable $B(\Gamma)$ to an applied time dependent external field is given by

$$\langle B(t) \rangle = \langle B(0) \rangle - \int_0^t ds \int d\Gamma B(\Gamma) \exp(-iL_0(t-s)) i\Delta L(s) f_0(\Gamma) \quad (6.8.12)$$

where iL_0 is the equilibrium (Nosé-Hoover thermostatted) f-Liouvillian and $i\Delta L(s) = iL(s) - iL_0$ where $iL(s)$ is the full field dependent thermostatted f-Liouvillian. It only remains to calculate $i\Delta L(s) f_0$. Using the equations of motion and the equilibrium distribution function obtained previously we see that,

$$\begin{aligned} i\Delta L(s) f_0 &= \left[\dot{\Gamma} \cdot \frac{\partial}{\partial \Gamma} + \dot{\xi} \frac{\partial}{\partial \xi} + \dot{\gamma} \frac{\partial}{\partial \gamma} \right] f_0 + f_0 \left[\frac{\partial}{\partial \Gamma} \cdot \dot{\Gamma} + \frac{\partial}{\partial \xi} \dot{\xi} + \frac{\partial}{\partial \gamma} \dot{\gamma} \right] \\ &= -\beta (\dot{H}_0 + \dot{\gamma} \gamma Q_\gamma + \dot{\xi} \xi Q_\xi) f_0 - 3N \dot{\xi} f_0 \\ &= \beta V S_{xy}(t) \gamma(\Gamma) f_0 \end{aligned} \quad (6.8.13)$$

Here we make explicit reference to the phase dependence of γ , and the explicit time dependence of the external field $S_{xy}(t)$. The quantity $-S_{xy}(t)V \gamma(\Gamma)$ is the adiabatic derivative of the extended internal energy, $E = H_0 + 1/2 Q_\gamma \gamma^2$.

Combining these results the linear response of the phase variable B is

$$\langle B(t) \rangle = \langle B(0) \rangle - \beta V \int_0^t ds \langle B(t-s) \gamma \rangle_0 S_{xy}(s) \quad (6.8.14)$$

In order to compute the shear viscosity of the system we need to calculate the time dependence of the thermodynamic force and flux which appear in the defining constitutive relation for shear viscosity. Because of the presence of the Nosé-Hoover relaxation time, controlled by the parameter Q_γ , the actual shear stress in the system $-P_{xy}(\Gamma)$, does not match the externally imposed shear stress $S_{xy}(t)$, instantaneously. To compute the shear viscosity we need to know the precise relation between P_{xy} and γ , not that between S_{xy} and the strain rate. The two quantities of interest are easily computed from (6.8.14).

$$\langle \gamma(t) \rangle = -\beta V \int_0^t ds \langle \gamma(t-s) \gamma \rangle_0 S_{xy}(s) \quad (6.8.15)$$

$$\langle P_{xy}(t) \rangle = -\beta V \int_0^t ds \langle P_{xy}(t-s) \gamma \rangle_0 S_{xy}(s) \quad (6.8.16)$$

Fourier-Laplace transforming we obtain the frequency dependent linear response relations

$$\langle \tilde{\gamma}(\omega) \rangle = -\tilde{\chi}_{\gamma\gamma}(\omega) \tilde{S}_{xy}(\omega) \quad (6.8.17)$$

$$\langle \tilde{P}_{xy}(\omega) \rangle = -\tilde{\chi}_{P_{xy}\gamma}(\omega) \tilde{S}_{xy}(\omega) \quad (6.8.18)$$

where the Fourier-Laplace transform of $\chi(t)$ is defined to be

$$\tilde{\chi}_{AB}(\omega) = \int_0^\infty dt \exp(-i\omega t) \chi_{AB}(t) = -\beta V \int_0^\infty dt \exp(-i\omega t) \langle A(t) B \rangle_0 \quad (6.8.19)$$

The linear constitutive relation for the frequency dependent shear viscosity is (§2.4),

$$\tilde{P}_{xy}(\omega) \equiv -\tilde{\eta}(\omega) \gamma(\omega) \quad (6.8.20)$$

so that the frequency dependent viscosity is

$$\tilde{\eta}(\omega) = -\frac{\tilde{\chi}_{P_{xy}\gamma}(\omega)}{\tilde{\chi}_{\gamma\gamma}(\omega)} \quad (6.8.21)$$

This expression shows that the complex frequency dependent shear viscosity is given by ratio of two susceptibilities. However, these two different time correlation functions can be related by using the Nosé-Hoover equation of motion (6.8.4),

$$\begin{aligned} \dot{\chi}_{\gamma\gamma}(t) &= -\beta V \langle \dot{\gamma}(t) \gamma \rangle_0 \\ &= -\frac{\beta V^2}{Q_\gamma} \langle P_{xy}(t) \gamma \rangle_0 \\ &= \frac{V}{Q_\gamma} \chi_{P_{xy}\gamma}(t) \end{aligned} \quad (6.8.22)$$

In the frequency domain this relation becomes,

$$\begin{aligned} \frac{V}{Q_\gamma} \tilde{\chi}_{P_{xy}\gamma}(\omega) &= -\chi_{\gamma\gamma}(t=0) + i\omega \tilde{\chi}_{\gamma\gamma}(\omega) \\ &= \frac{V}{Q_\gamma} + i\omega \tilde{\chi}_{\gamma\gamma}(\omega) \end{aligned} \quad (6.8.23)$$

The frequency dependent shear viscosity in the constant stress ensemble can be written as,

$$\tilde{\eta}(\omega) = -\frac{1 + \frac{i\omega Q_\gamma \tilde{\chi}_{\gamma\gamma}(\omega)}{V}}{\tilde{\chi}_{\gamma\gamma}(\omega)} \quad (6.8.24)$$

In a similar way it is possible to write the frequency dependent viscosity in terms of either the Norton ensemble stress autocorrelation function, or the Norton ensemble stress-strain cross correlation function. Using equation (4.1.10), the stress autocorrelation function can be related to the strain autocorrelation function using the relation,

$$\frac{d^2}{dt^2} \chi_{\gamma\gamma}(t) = -\frac{V^2}{Q_\gamma^2} \chi_{P_{xy}P_{xy}}(t) \quad (6.8.25)$$

In the frequency domain this becomes,

$$\tilde{\chi}_{\gamma\gamma}(\omega) = -\frac{V}{i\omega Q_\gamma} \left(1 + \frac{V}{i\omega Q_\gamma} \tilde{\chi}_{P_{xy}P_{xy}}(\omega) \right) \quad (6.8.26)$$

Substituting this equation into (6.8.24) gives,

$$\tilde{\eta}(\omega) = \frac{-\tilde{\chi}_{P_{xy}P_{xy}}(\omega)}{1 + \frac{V}{i\omega Q_\gamma} \tilde{\chi}_{P_{xy}P_{xy}}(\omega)} \quad (6.8.27)$$

In terms of the cross correlation function, the frequency dependent viscosity is

$$\tilde{\eta}(\omega) = -\frac{i\omega Q_\gamma}{V} \frac{\tilde{\chi}_{P_{xy}\gamma}(\omega)}{\tilde{\chi}_{P_{xy}\gamma}(\omega) - 1} \quad (6.8.28)$$

In Figure 6.14 we show the results of a test of the theory given above. Hood, Evans and Morriss (1987) computed the strain rate autocorrelation function in the Norton ensemble and the stress autocorrelation function in the Thévenin ensemble. They then used equation (6.8.24) to **predict** the strain rate autocorrelation function on the basis of their Thévenin ensemble data. The system studied was the Lennard-Jones triple point fluid. The smooth curves denote the autocorrelation function computed in the Norton ensemble and the points give the predictions from the Thévenin ensemble data. The two sets of data are in statistical agreement. This analysis shows that in spite of the fact that the damping constant Q_γ , has a profound influence on the time dependent fluctuations in the system, the theory given above correctly relates the Q_γ -dependent fluctuations of strain rate and stress to the Q_γ -**independent**, frequency dependent viscosity

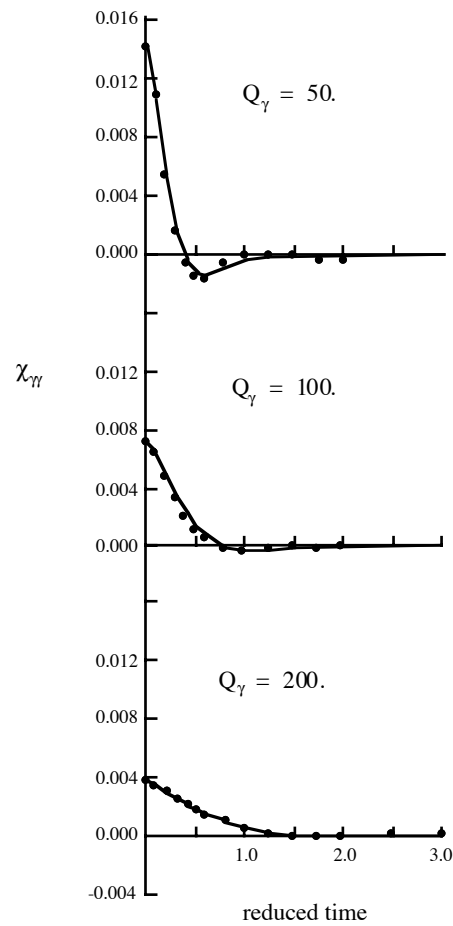


Figure 6.14

Figures 6.15-17 show the various Norton ensemble susceptibilities as a function of frequency. The system is the Lennard-Jones triple point fluid.

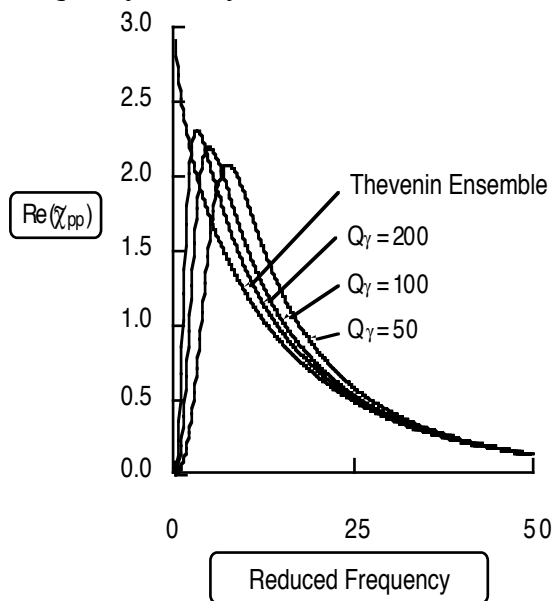


Figure 6.15

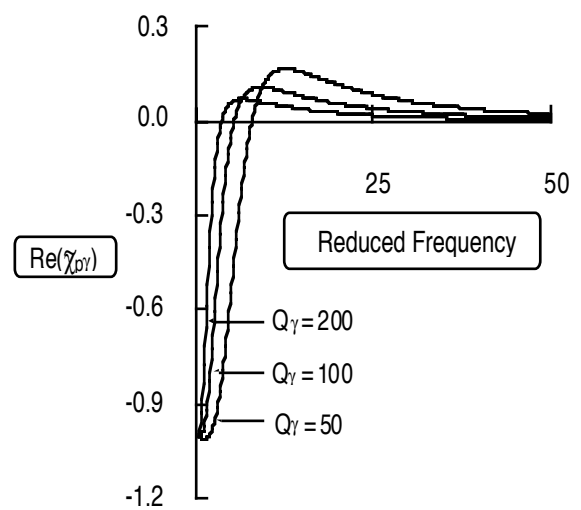
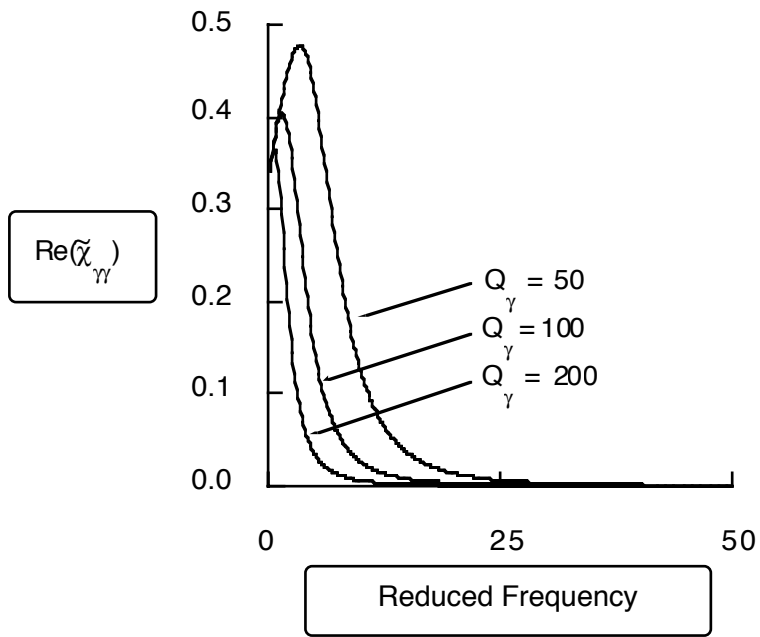


Figure 6.16

**Figure 6.17**